

Supporting Information

Deciphering the alternating synergy between interlayer Pt single-atom and NiFe layered double hydroxide for overall water splitting

Wei Chen,^{‡a} Binbin Wu,^{‡a} Yanyong Wang,^{‡a} Wang Zhou,^{‡b} Yingying Li,^{‡a} Tianyang Liu,^{‡c} Chao Xie,^a Leitao Xu,^a Shiqian Du,^a Minglei Song,^a Dongdong Wang,^a Yanbo liu,^a Yefei Li,^d Jilei Liu,^b Yuqin Zou,^a Ru Chen,^{*a} Chen Chen,^a Jianyun Zheng,^a Yafei Li,^{*c} Jun Chen^{*e} and Shuangyin Wang^{*a}

Experimental Procedures

Chemicals. All chemical reagents were purchased from Sigma-Aldrich (St Louis, MO, USA) or Sinopharm Chemical Reagent Co.,Ltd (Shanghai, Mainland) without further purification. The carbon cloth (HCP330P) was purchased from ShangHai Hesen Electrical Appliance Co. Ltd.

Materials fabrication.

Synthesis of Ni₃Fe-CO₃²⁻ LDH with different size. 15 mmol Ni(NO₃)₂·6H₂O and 5 mmol Fe(NO₃)₃·9H₂O were dissolved in 40 mL deionized water. 60 mmol NaCO₃, as precipitator, was dissolved in 40 mL deionized water. After stirring for 30 minute, NaCO₃ solution was dribbled into the mixed solution with vigorous stirring. Brown suspension was obtained and continued to whisk for 30 minute. Then the suspension was poured into a 100 mL Teflon-lined stainless steel autoclave. In order to adjust the size of NiFe LDH, Teflon-lined stainless steel autoclave was heated at 60, 90 and 120 °C for 10 hours. By the time stainless steel autoclave cooled down naturally to room temperature, samples were washed with deionized water and anhydrous ethanol for six times. After vacuum drying at 60°C for 10 hours, Ni₃Fe-CO₃²⁻ LDH samples with different size were synthesized successfully. Given the nickel-iron hydroxides suspension with high pH, there are reasons for thinking all the Ni and Fe cations are converted to hydroxide sediment. Hence, it is reasonable that the naming of Ni₃Fe-CO₃²⁻ LDH originates from the ratios in the precursors used in the hydrothermal synthesis.

Synthesis of Ni_xM-PtCl₆²⁻ LDH (M = Co, Fe, Al). With Ni_xM-CO₃²⁻ LDH as the precursor, anion exchange method was adopted to Ni_xM-PtCl₆²⁻ LDH. Deionized water was treated by boiling to remove dissolved CO₂. 1 mL solution with 20 mg Na₂PtCl₆·6H₂O was poured into 50 mL the deionized water without dissolved CO₂, and pH of the mixed solution was reduced to 4 by hydrochloric acid. A weakly acidic environment can promote the hydrolysis of CO₃²⁻, so that, under the electrostatic adsorption of Fe³⁺ in layer plates of LDH, PtCl₆²⁻ can enter confined space in LDH easier. 50 mg Ni_xM-CO₃²⁻ LDH was dispersed in aforementioned solution and formed a uniform suspension with stirring. After stirring for 12 hours under the protection of nitrogen, intercalation CO₃²⁻ of Ni_xM-CO₃²⁻ LDH was replaced by PtCl₆²⁻. Subsequently, Ni_xM-PtCl₆²⁻ LDH, obtained through filtering, were washed with deionized water and anhydrous ethanol for six times. After vacuum drying at 60°C for 10 hours, Ni_xM-PtCl₆²⁻ LDH were synthesized successfully.

Synthesis of Ni_xM-CO₃²⁻ LDH-Pt single-atom (M = Co, Fe, Al). Ni_xM³⁺-CO₃²⁻ LDH-Pt SA was synthesized through electrochemical reduction. In 1 M KOH, Ni_xM-PtCl₆²⁻ LDH electrode was adopted as cathode. At

reduction potential, electroreduction could remove Cl ligand of intercalation PtCl_6^{2-} and anchor Pt single-atom swiftly. For $\text{Ni}_x\text{M-CO}_3^{2-}$ LDH-Pt single-atom preparation on the glassy carbon electrode, LSV curves was measured from 0.15 to -0.2 V with the scan rate of 5 mV s^{-1} . Until HER performance was stable, $\text{Ni}_x\text{M}^{3+}\text{-CO}_3^{2-}$ LDH-Pt SA was synthesized successfully. In fact, for fabricating $\text{Ni}_x\text{M}^{3+}\text{-CO}_3^{2-}$ LDH-Pt SA, the electroreduction method has a good adaptability due to the unique structure of SAC precursor ($\text{Ni}_x\text{M}^{3+}\text{-PtCl}_6^{2-}$ LDH); $\text{Ni}_x\text{M}^{3+}\text{-CO}_3^{2-}$ LDH-Pt SA can be synthesized quickly under suitable conditions of electroreduction. In this work, most LSV curves were iR-corrected according to the equation ($E_{\text{iR-corrected}} = E - I \times R_s$). However, for the $\text{Ni}_x\text{M-CO}_3^{2-}$ LDH-Pt single-atom preparation, the solution resistance (R_s) was not eliminated. The geometric areas of the glassy carbon electrode and the glassy carbon plate electrode are 0.196 and 1 cm^2 , respectively. For bigger area electrode, the current will be larger and R_s will be lower. The current of the glassy carbon plate electrode (1 cm^2) is nearly five times that of the glassy carbon electrode (0.196 cm^2) at the same actual potential. The electrolyte resistances of the glassy carbon electrode (0.196 cm^2) and the glassy carbon plate electrode (1 cm^2) are $\sim 2 \Omega$ and $\sim 3 \Omega$, respectively. According to the equation ($E = E_{\text{iR-corrected}} + I \times R_s$), when the influence of the solution resistance (R_s) to the measurement has not been eliminated, the enlargement of potential window is needed for the glassy carbon plate electrode (1 cm^2) with larger current. It is worth noting that the $\text{Ni}_3\text{Fe-CO}_3^{2-}$ LDH-Pt single-atom preparation on the glassy carbon plate electrode (1 cm^2) was used mainly in the XPS measurements. Hence, for $\text{Ni}_3\text{Fe-CO}_3^{2-}$ LDH-Pt single-atom preparation on the glassy carbon plate electrode (1 cm^2), LSV curves was measured from 0.15 to -0.3 V with the scan rate of 50 mV s^{-1} .

Synthesis of $\text{Ni}_x\text{M-CO}_3^{2-}$ LDH (M = Co, Fe, Al). $\text{Ni}_9\text{Fe-CO}_3^{2-}$ LDH, $\text{Ni}_{95}\text{Fe}_5\text{-CO}_3^{2-}$ LDH, $\text{Ni}_3\text{Al-CO}_3^{2-}$ LDH and $\text{Ni}_2\text{CoFe-CO}_3^{2-}$ LDH were synthesized in the same coprecipitation method with $60 \text{ }^\circ\text{C}$ hydrothermal temperature.

Synthesis of $\text{Ni}_3\text{Fe LDH-Pt NP}$. $\text{Ni}_3\text{Fe LDH-Pt NP}$ was synthesized through thermal reduction. Under 10% H_2/Ar atmosphere, $\text{Ni}_3\text{Fe-PtCl}_6^{2-}$ LDH was heated at $150 \text{ }^\circ\text{C}$ for 30 minute in tube furnace. Both heating and cooling rates were maintained at $2 \text{ }^\circ\text{C}/\text{min}$. After thermal reduction, intercalation PtCl_6^{2-} anions were reduced to Pt nanoparticles in $\text{Ni}_3\text{Fe LDH}$, meanwhile, $\text{Ni}_3\text{Fe LDH}$ could not be reduced, thereby gaining $\text{Ni}_3\text{Fe LDH-Pt NP}$.

Synthesis of Pt nanoparticle/ $\text{Ni}_3\text{Fe LDH}$. In order to identify the relationship between HER activity and state of Pt atoms, 10 wt% Pt nanoparticles loading on surface of $\text{Ni}_3\text{Fe-CO}_3^{2-}$ LDH (Pt NP/ $\text{Ni}_3\text{Fe LDH}$) was synthesized. 45 mg $\text{Ni}_3\text{Fe-CO}_3^{2-}$ LDH and 14.7 mg $\text{Na}_2\text{PtCl}_6 \cdot 6\text{H}_2\text{O}$ were dispersed in 50 mL deionized water

with stirring. 20 mg NaBH_4 was dissolved in 20 mL deionized water. The dilute solution of NaBH_4 was then pumped into the suspension in rate of 1 mL/min with vigorously stirring. Subsequently, Pt NP/ Ni_3Fe LDH, obtained through filtering, were washed with deionized water and anhydrous ethanol for six times. After vacuum drying at 60°C for 10 hours, Pt NP/ Ni_3Fe LDH was synthesized successfully.

Characterization.

The structure and morphology were characterized by transmission electron microscope (TEM, FEI Tecnai G20) and X-ray diffraction (XRD, Bruker D8 Advance diffractometer, $\text{Cu K}\alpha 1$). The HAADF-STEM and ABF-STEM images were obtained by a probe-corrected JEOL ARM200F. The BET surface area was measured by JWGB JW-BK200C. X-ray photoelectron spectroscopy (XPS) was tested by AXIS Supra (Axis Supra, Kratos, England). All XPS spectra were adjusted by C 1s (284.8 eV). It's worth noting that, for the XPS measurement of $\text{Ni}_3\text{Fe-PtCl}_6^{2-}$ LDH electrodes with varying degrees of electroreduction in this work, the time lag between sample preparation and XPS measurement was shortened as much as possible. FTIR spectra were carried out by Bruker Tensor II. The confocal Raman microscope (Alpha300R, WETEC, Germany) was used to measure in situ and ex situ Raman spectrum. Operando electrochemical impedance spectroscopy (EIS) was carried out by Autolab PGSTAT302N (Eco Chemie, Utrecht, Netherlands) with frequency range from 1 M Hz to 0.1 Hz.

Electrochemical Measurements.

Almost all of the electrochemical measurements were measured on electrochemical workstation (CHI 760D) except operando EIS. In order to show a fair comparison of electrochemical performances, all electrocatalysts were measured on glassy carbon electrode or glassy carbon plate electrode. For glassy carbon electrode and glassy carbon plate electrode, the geometric areas are 0.196 and 1cm^2 , respectively. During electrode fabrication, firstly, 4 mg electrocatalyst was dispersed in 950 μL deionized water. Secondly, after ultrasonic dispersion for 20 minute, 50 μL 5 wt% Nafion solution was added to homogeneous suspension and continued to ultrasonic dispersion for 20 minute. Finally, suspension was dropped on a glassy carbon electrode and slowly dried, and preparative thin film electrode glassy carbon ($0.2\text{ mg electrocatalyst cm}^{-2}$) was utilized in subsequent electrochemical measurements. For characterization about C or O element (such as XPS and Raman spectra), during electrode fabrication, Nafion would not be added in order to avoid interference. The three-electrode configuration was adopted during electrochemical tests with carbon rod as counter electrode. For electrochemical measurements in 1 M KOH, Hg/HgO electrode was selected as reference electrode;

however, in 0.1 M HClO₄, saturate calomel electrode (SCE) was selected as reference electrode. Before electrochemical measurements in different electrolytes, the reference electrode was corrected through testing the reversible hydrogen electrode (RHE) potential with platinum gauze electrode as work electrode in corresponding hydrogen-saturated electrolyte solution. For HER and OER, electrochemical measurements were carried out in hydrogen-saturated and oxygen-saturated electrolyte solution, respectively. 20 and 40 wt% commercial Pt/C were purchased from Johnson Matthey Co. Ltd. For HER and OER performances, the scan rate of 5 mV s⁻¹ was adopted to eliminate the interference of capacitance, meanwhile, stable LSV curve was recorded as performance. The thermostatic water bath (25 °C) was used in subsequent all tests. Part of test was measured on the rotating disk electrode with 1600 rpm (CPR+Wavenow, PINE, America). Besides electroreduction, most LSV curves were iR-corrected according to the following equation.

$$E_{iR\text{-corrected}} = E - I \times R_s$$

Turnover frequency.

In order to calculate TOF_{Bulk}, TOF_{Surface} and TOF_{Redox}, the following equation is fundamental formula for reference:

$$\text{TOF} = \text{Production rate of O}_2 \div \text{Number of active sites}$$

Production rate of O₂ (cm⁻² s⁻¹) was calculated through the following equation:

$$\text{Production rate of O}_2 = (I \times N_A) \div (z \times F)$$

Where I (A cm⁻²) is the current density, N_A is the Avogadro number (6.02×10²³ mol⁻¹), z (4) is the number of electrons for OER and F is the Faraday constant (96485C mol⁻¹).

Production rate of O₂ is explicit without dispute; however, it is difficult to identify the number of active sites (cm⁻²) because of vague OER mechanism.

For TOF_{Bulk}, it is assumed that all specific metal atoms are OER active sites.

$$\text{Number of active sites} = m \times N_1$$

Where m (0.0002 g cm⁻²) is load of electrocatalyst and N₁ (g⁻¹) is customized constant representing number of active sites per gram of electrocatalyst. Besides, n₁ is a non-dimensional constant, and its value is equal to N₁ (g⁻¹).

For Ni₃Fe LDH with different size, we consider that n₁ is invariable, meanwhile, compared with vague TOF_{Bulk}, the number of N₁ × TOF_{Bulk} is explicit without dispute. Hence, the number of n₁ × TOF_{Bulk} is selected to measure TOF_{Bulk}.

$$N_1 \times \text{TOF}_{\text{Bulk}} = (I \times N_A) \div (z \times F \times m)$$

For $\text{TOF}_{\text{Surface}}$, it is assumed that specific surface metal atoms are OER active sites.

$$\text{Number of active sites} = m \times S_g \times N_2$$

Where m (0.0002 g cm^{-2}) is load of electrocatalyst, S_g ($\text{m}^2 \text{ g}^{-1}$) is corresponding to BET specific surface area and N_2 (m^{-2}) is customized constant representing number of active sites per square meter of electrocatalyst surface. Besides, n_2 is a non-dimensional constant, and its value is equal to N_2 (m^{-2}).

For Ni_3Fe LDH with different size, we consider that n_2 is invariable, meanwhile, compared with vague $\text{TOF}_{\text{Surface}}$, the number of $N_2 \times \text{TOF}_{\text{Surface}}$ is explicit without dispute. Hence, the number of $n_2 \times \text{TOF}_{\text{Surface}}$ is selected to measure $\text{TOF}_{\text{Surface}}$.

$$N_2 \times \text{TOF}_{\text{Surface}} = (I \times N_A) \div (z \times F \times m \times S_g)$$

For $\text{TOF}_{\text{Redox}}$, it is assumed that specific metal atoms in oxide layer are OER active sites.



So we quantify the number of oxide layer through integrating charge (Q_{Redox}) of reduction peak from Ni^{3+} to Ni^{2+} . In view of the number of oxide layer species, number of active sites is shown as following.

$$\text{Number of active sites} = (Q_{\text{Redox}} \times N_A) \div (z_2 \times F)$$

Where Q_{Redox} (C cm^{-2}) is number of oxide layer species, z_2 (1) is the number of electrons for electrocatalyst electrooxidation reaction.

$\text{TOF}_{\text{Redox}}$ is explicit without dispute.

$$\text{TOF}_{\text{Redox}} = I \div (z \times Q_{\text{Redox}})$$

DFT calculations.

The spin-polarized density functional theory (DFT) computations were performed in the Vienna ab initio simulation package (VASP).^[1] The convergence threshold were set to 5×10^{-5} eV in energy and 0.05 eV/Å for the force, respectively. And a cut-off energy of 420 eV for the plane-wave basis set were adopted in all computations.^[2] Hubbard U correction was employed (DFT +U) using the generalized gradient approximation (GGA) of Perdew–Burke–Ernzerhof (PBE) methods to account for the correlation energy of the strongly localized 3d orbital.^[3] In this work, setting the U-J=3.5 eV for Fe, U-J=6 eV for Ni, respectively. Brillouin zone was represented by the Monkhorst–Pack special k-point mesh of $3 \times 3 \times 1$ and $7 \times 7 \times 1$ for geometry optimization and electronic structure computations. DFT-D3 (D stands for dispersion) procedure to be expressed van der Waals (vdW) interactions.^[4] In order to calculate accurately, the solvation effects also considered with the

Poisson–Boltzmann implicit solvation model, and the dielectric constant of water was taken as 80.^[5]

In detail, the adsorption free energy (ΔG_{ads}) was calculated by following formula:

$$\Delta G_{ads} = \Delta E_{ads} + \Delta E_{ZPE} - T\Delta S \quad (S1)$$

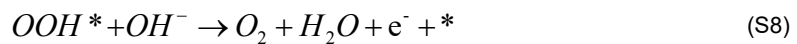
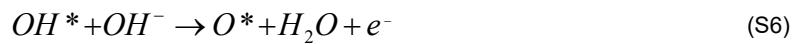
Where E was defined as the total energies, E_{ZPE} and TS were defined as zero-point energy and entropy correct, respectively. Furthermore, the OER intermediates for OER (OOH^* , O^* , OH^*) were determined by the following equation:

$$\Delta G_{OOH^*} = G_{OOH^*} - G_* - (2G_{H_2O} - 2/3G_{H_2}) \quad (S2)$$

$$\Delta G_{O^*} = G_{O^*} - G_* - (G_{H_2O} - G_{H_2}) \quad (S3)$$

$$\Delta G_{OH^*} = G_{OH^*} - G_* - (G_{H_2O} - 1/2G_{H_2}) \quad (S4)$$

At alkaline environment, the 4e⁻ step OER process can be written as follow:



Where * represents an adsorption site on the surface. Then, the free energy of all the OER steps can be expressed as:

$$\Delta G_1 = \Delta G_{OH^*} \quad (S9)$$

$$\Delta G_2 = \Delta G_{O^*} - \Delta G_{OH^*} \quad (S10)$$

$$\Delta G_3 = \Delta G_{OOH^*} - \Delta G_{O^*} \quad (S11)$$

$$\Delta G_4 = 4.92 - \Delta G_{OOH^*} \quad (S12)$$

The most positive free energy change step was potential determine step and the theoretical overpotential U_o

was defined in equation:

$$U_o = \max \{ \Delta G_1, \Delta G_2, \Delta G_3, \Delta G_4 \} / e - 1.23 \text{ V} \quad (\text{S13})$$

In situ XAS measurements.

X-ray absorption spectroscopy composed of X-ray absorption near edge spectra (XANES) and extended X-ray absorption fine structure (EXAFS) was carried out to obtain material structure of a given material and the oxidation state of certain elements by measuring the X-ray absorption coefficient as a function of X-ray photon energy. Researchers are increasingly recognizing the complementary nature of XAS technology to XRD, and have been widely used in the structural studies of catalytic material.^[6] In situ XAS reveals the redistribution of dynamic electron charge, the movement of the conduction band edge, the change of unoccupied state density, and the improvement of electrocatalytic activity, so this has been extensively studied. Specifically, for EXAFS, X-ray that determine energy are absorbed and excite core electrons.

In situ EXAFS measurement was conducted at the Taiwan Photon Source (TPS), NSRRC (National Synchrotron Radiation Research Center). The Quick-Scanning XAS beamline, BL44A, is a hard X-ray bending magnet beamline covering energy range of 4.5 – 34 keV that provides the capability of the fast scanning for in situ time-resolved XAFS measurements.^[7] A full Quick-Scanning XAFS spectrum can be obtained in less than 100 milliseconds over an energy range over 1000 eV. X-ray absorption measurements of Ni K-edge (8,333 eV) and Fe K-edge (7,112 eV) using synchrotron radiation in transmission mode at ambient air/temperature. The energy resolutions of Ni K-edge and Fe K-edge XANES were set to ~ 0.4 and 0.35 eV, respectively. XANES uses standard procedures, including background subtraction and normalized edge height, while EXAFS uses k^3 -weighted oscillation Fourier transform to estimate to obtain the local environment of Ni and Fe atoms. In addition, its transmission mode also makes operation detection possible. In general, the advantages of data collection and interpretation make Quick-XAFS easier, so that immediate XAS can observe signals without bubble interference.

Since the catalytic properties depend strongly on the electrical state of the relevant reaction catalyst, so if the surface of the reaction can be monitored in the liquid condition of the structure, it would be highly desirable. In order to reduce the noise generated by the gas, obtain a stable surface state signal and monitor the catalyst in the liquid environment. We designed a hard X-ray liquid reaction cell, which composed of a Kapton polyimide film with a thickness of 0.06 mm served as X-ray window and the cell was made of Teflon line. An in situ transmission mode X-ray absorption method can be implemented in a liquid environment to determine the atomic structure of the catalyst surface under ambient conditions, especially for high voltage out gassing

production.

In this experiment, to balance the signal-to-noise ratio and Ni₃Fe LDHs powder was dropwise add to homogeneous suspension with 50 μ L 5 wt% Nafion solution, and continued to ultrasonic dispersion for 20 minutes, the data acquisition frequency is set to 0.5 seconds per spectrum. In order to ensure the working catalysts reaching a steady state during in situ characterization, every single characterization is already followed by 5 minutes electrolysis. Quick-XAFS scans produce a large volume of data. The compiling of the data is conducted on-site using a customized data processing program. It allows user either to export each EXAFS scan as a single file, or to combine several consecutive scans into one file. In the current analysis, each output data is a combination of 240 scans, which covers the time window of 120 s. The data was then processed with ATHENA for energy alignment and normalization.^[8]

The ex situ XAS analysis will also be able to provide rich information on the change of local chemical environment in this case. In the following, our analysis is focused on the XANES at the Pt K-edge. Linear combination fit of XANES was conducted between -50 eV and 200 eV relative to E₀ using the ATHENA program. Commercially obtained Pt foil, PtO₂ powder and H₂PtCl₆ a pellet are used as references for Pt(0), Pt(IV) and precursor, respectively.

The XAS were performed at beamline BL44A at the TPS using step-by-step mode (s-scan) or on-the-fly mode (q-scan). The storage ring was operated at 3.0 GeV with top-up beam current at 450 mA. *In situ* XAS were carried out under catalytic conditions using a home-made electrochemical cell. All spectra were collected with 1Hz oscillating frequency for 5min. Thus, one spectrum is an average of six hundred scans to ensure the good S/N ratio. Raw data were analyzed following standard procedures, including pre-edge and post-edge background subtractions, normalization with respect to the edge jump, Fourier transformation and non-linear least-squares curve fitting. The XAS data were analyzed using the standard program Demeter and the detailed description of the procedure is given elsewhere. The backscattering amplitude and phase shift for specific atom pairs were obtained from ab initio calculation using the FEFF6 code. The Ni K-edge and Fe K-edge XAS were recorded in transmission mode using q-scan via QEXAFS recorder system. For the low concentrated samples, fluorescence mode is applied. The Pt L₃-edge spectra were collected in fluorescence mode using s-scan, a pin diode is used as a fluorescence detector. For the samples with very low elemental concentrations (can be as low as ppm level), a seven-element silicon drift detector (SDD) is used in the s-scan mode. For the s-scans, the voltage signals from the current amplifiers are converted into frequencies using voltage-to-frequency converters (Tsuji Electronics VF8-01) and digitized using a counter (Tsuji Electronics

Supporting Figures

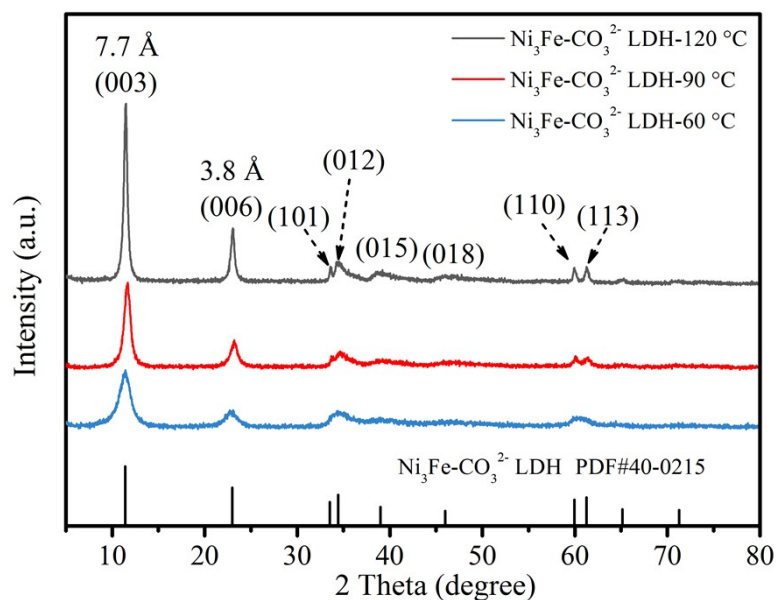


Figure S1. XRD patterns of $\text{Ni}_3\text{Fe-CO}_3^{2-}$ LDHs with different size and thickness. All peaks of these samples accord with $\text{Ni}_3\text{Fe-CO}_3^{2-}$ LDH phase (PDF#40-0215). Through comparing the full width at half-maximum of (003) and (006) diffraction peaks based on Debye-scherrer formula, it proves that $\text{Ni}_3\text{Fe-CO}_3^{2-}$ LDHs with different sizes and thicknesses have been synthesized successfully by regulating the hydrothermal temperature.

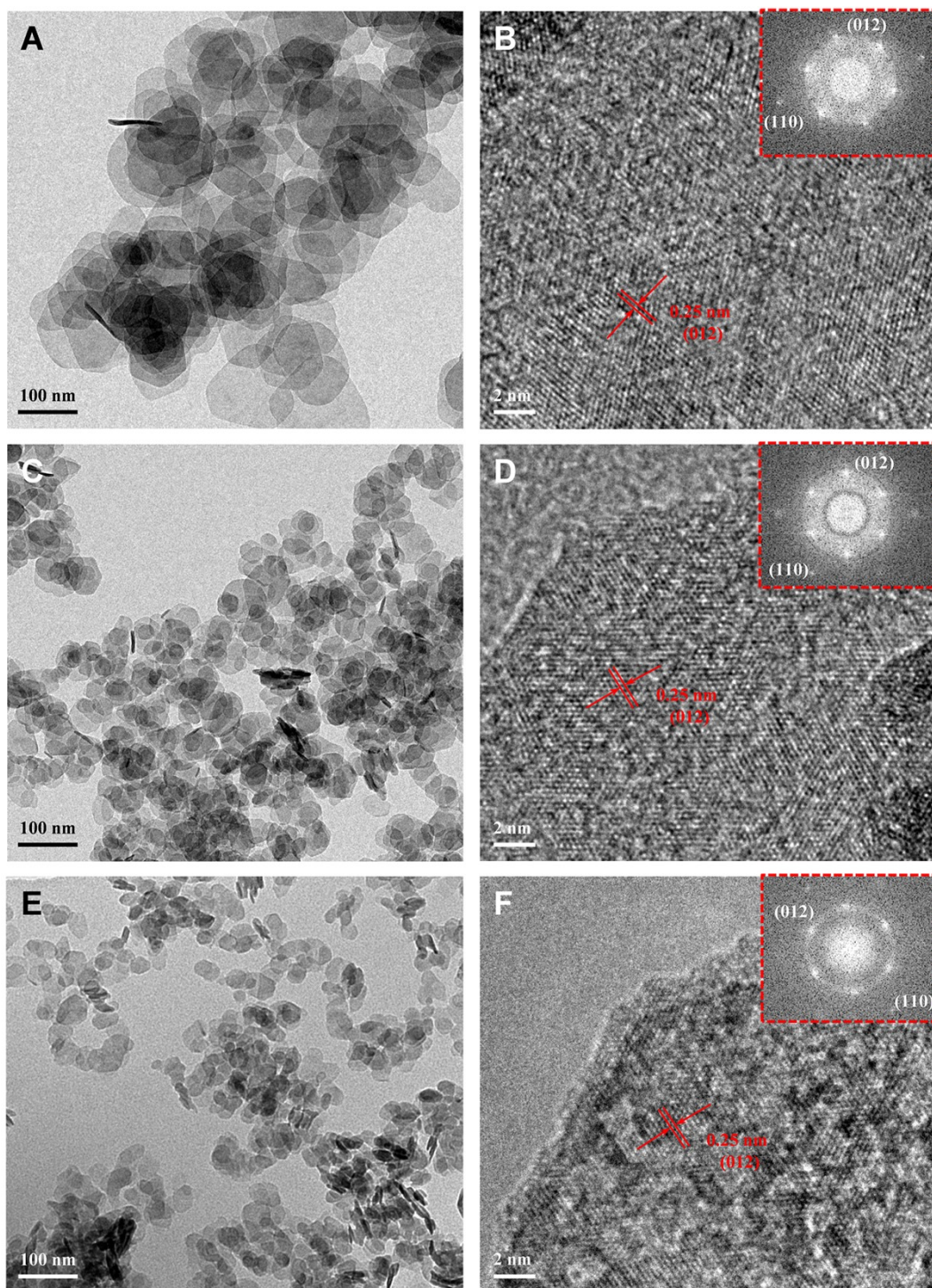


Figure S2. TEM images and corresponding electronic diffraction patterns of (A and B) $\text{Ni}_3\text{Fe-CO}_3^{2-}$ LDH-120 °C, (C and D) $\text{Ni}_3\text{Fe-CO}_3^{2-}$ LDH-90 °C and (E and F) $\text{Ni}_3\text{Fe-CO}_3^{2-}$ LDH-60 °C. For $\text{Ni}_3\text{Fe-CO}_3^{2-}$ LDHs were synthesized in 120, 90 and 60 °C, their sizes of layer plate are 120 to 180 nm, 80 to 120 nm and 40 to 60 nm, respectively. The lattice spacings are found to be 0.25 nm corresponding to the distance of (012) lattice plane of $\text{Ni}_3\text{Fe-CO}_3^{2-}$ LDH.

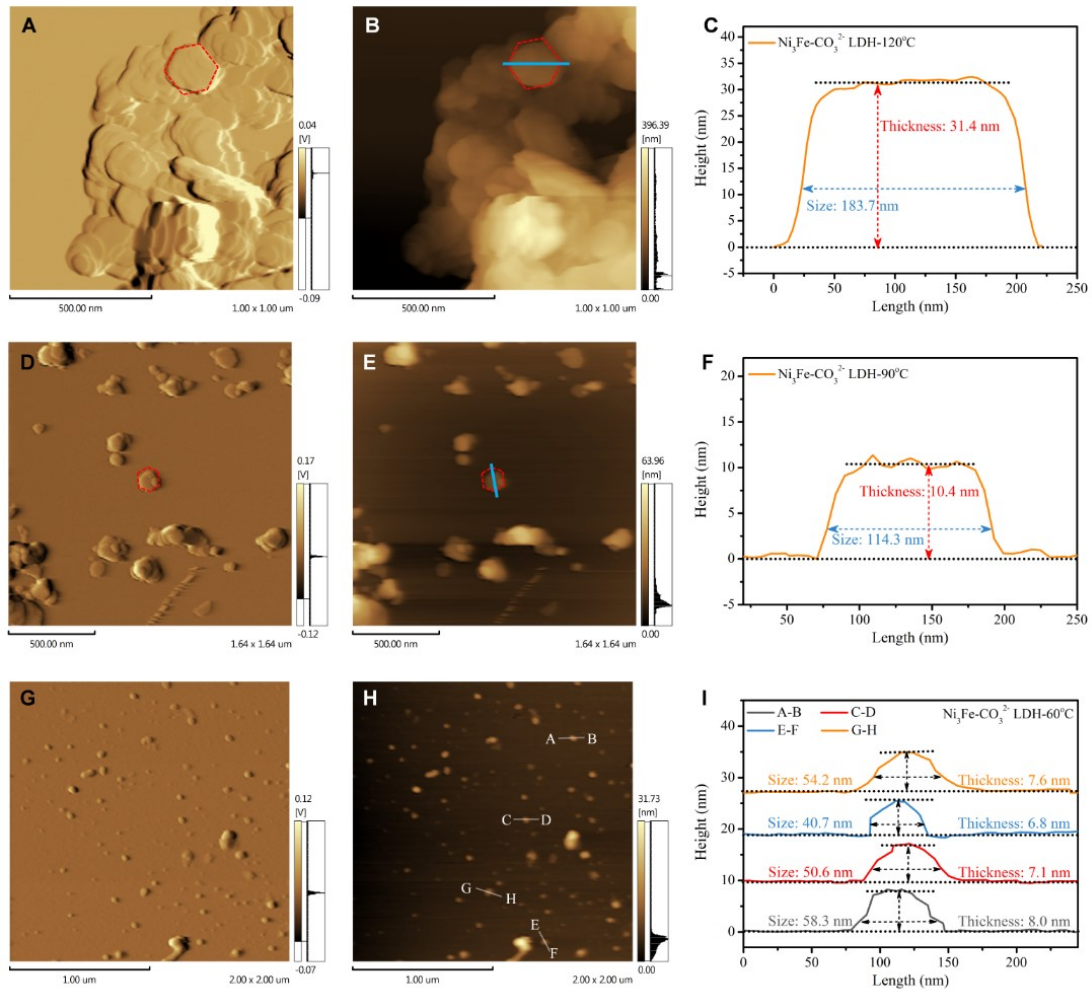


Figure S3. AFM images and the corresponding height profiles of (A, B and C) $\text{Ni}_3\text{Fe-CO}_3^{2-}$ LDH-120 °C, (D, E and F) $\text{Ni}_3\text{Fe-CO}_3^{2-}$ LDH-90 °C and (G, H and I) $\text{Ni}_3\text{Fe-CO}_3^{2-}$ LDH-60 °C. For $\text{Ni}_3\text{Fe-CO}_3^{2-}$ LDHs synthesized in 120, 90 and 60 °C, their sizes of layer plate accord with TEM images. Thereinto, for $\text{Ni}_3\text{Fe-CO}_3^{2-}$ LDH-120 °C and $\text{Ni}_3\text{Fe-CO}_3^{2-}$ LDH-90 °C, their thicknesses are 31.4 and 10.4 nm, respectively. For $\text{Ni}_3\text{Fe-CO}_3^{2-}$ LDH-60 °C nanosheets, AFM line-scan images for several nanosheets show that their sizes and thicknesses are ~50 and ~7 nm, respectively.

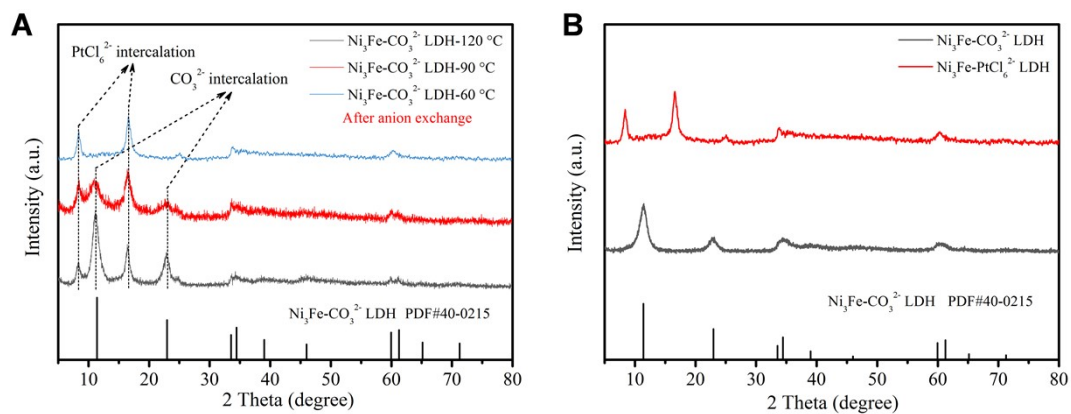


Figure S4. (A) XRD patterns of Ni_3Fe LDH intercalated with PtCl_6^{2-} which were synthesized by anion exchange with $\text{Ni}_3\text{Fe-CO}_3^{2-}$ LDH-120 °C, $\text{Ni}_3\text{Fe-CO}_3^{2-}$ LDH-90 °C and $\text{Ni}_3\text{Fe-CO}_3^{2-}$ LDH-60 °C as precursors. (B) XRD patterns of $\text{Ni}_3\text{Fe-CO}_3^{2-}$ LDH and $\text{Ni}_3\text{Fe-PtCl}_6^{2-}$ LDH.

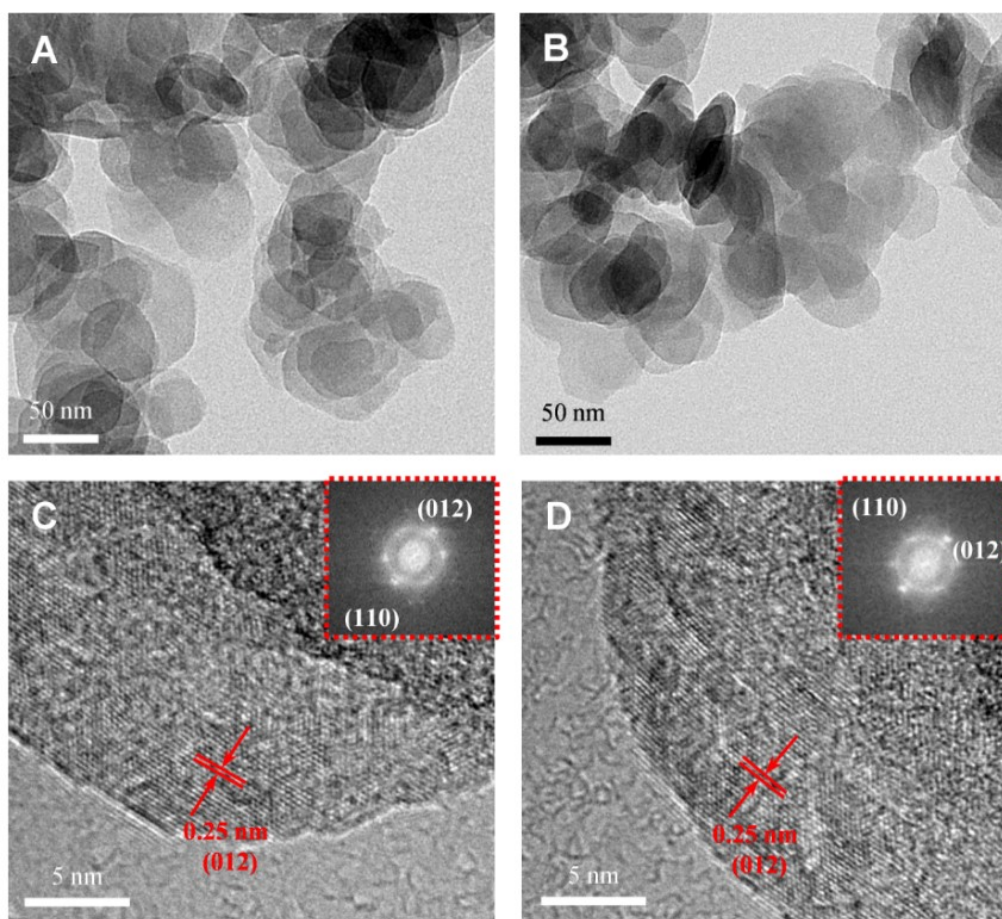


Figure S5. TEM images and the corresponding electronic diffraction patterns of $\text{Ni}_3\text{Fe-PtCl}_6^{2-}$ LDH. The lattice spacings are found to be 0.25 nm corresponding to the distance of (012) lattice plane of $\text{Ni}_3\text{Fe-PtCl}_6^{2-}$ LDH.

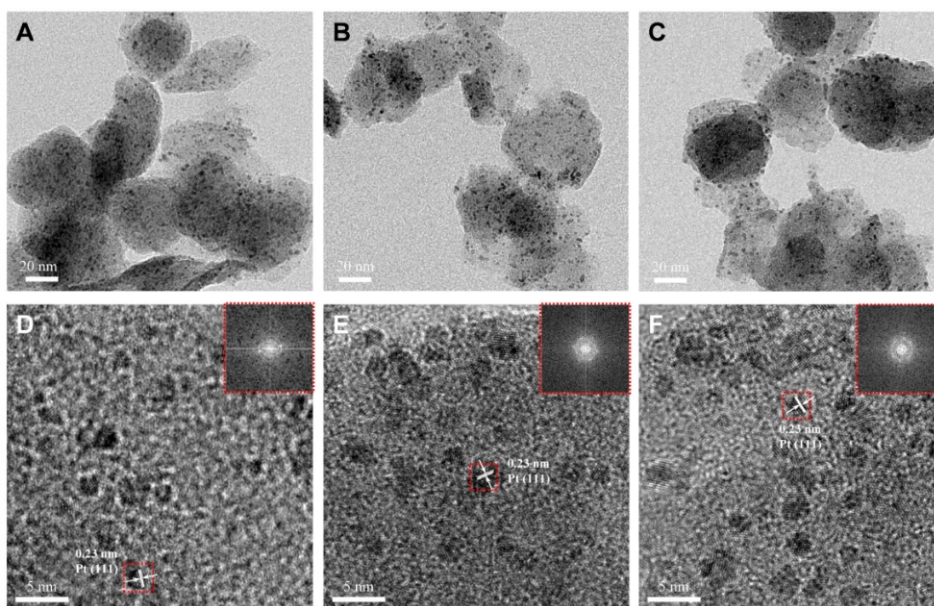


Figure S6. TEM images and the corresponding electronic diffraction patterns of Ni₃Fe LDH-Pt NP. After thermal reduction, interlayer PtCl₆²⁻ anions in Ni₃Fe-PtCl₆²⁻ LDH were reduced to Pt nanoparticles. The lattice spacings are found to be 0.23 nm corresponding to the distance of (111) lattice plane of Pt nanoparticles.

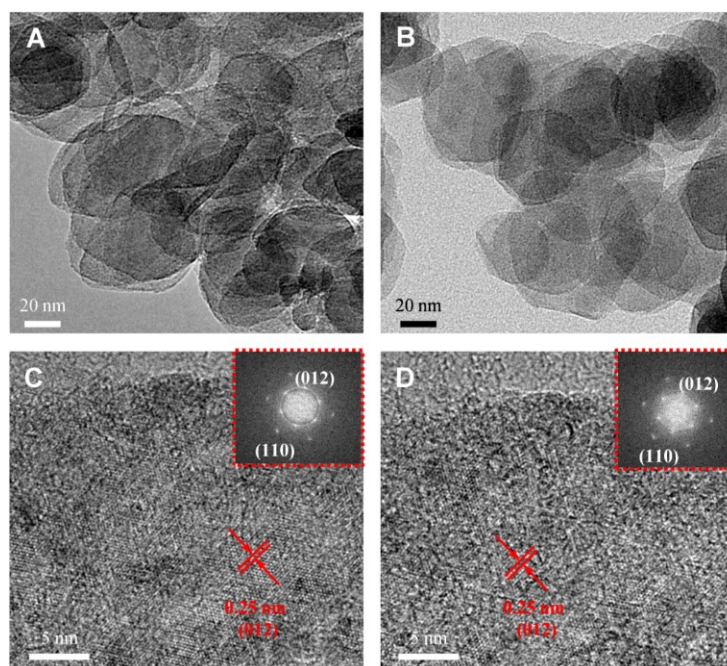


Figure S7. TEM images and the corresponding electronic diffraction patterns of Ni₃Fe-CO₃²⁻ LDH-Pt SA. After electrochemical reduction of Ni₃Fe-PtCl₆²⁻ LDH, interlayer PtCl₆²⁻ anions were not reduced to Pt nanoparticles. Electronic diffraction patterns show that, after electrochemical reduction, layer plate structure of Ni₃Fe-CO₃²⁻ LDH-Pt SA remains high crystalline similar as Ni₃Fe-CO₃²⁻ LDH precursor.

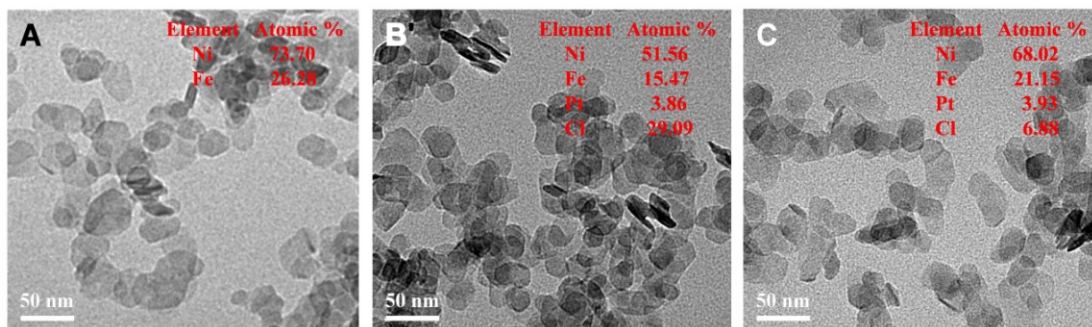


Figure S8. TEM images of (A) $\text{Ni}_3\text{Fe-CO}_3^{2-}$ LDH, (B) $\text{Ni}_3\text{Fe-PtCl}_6^{2-}$ LDH and (C) $\text{Ni}_3\text{Fe-CO}_3^{2-}$ LDH-Pt SA. Insets show the atom ratio by EDS analysis

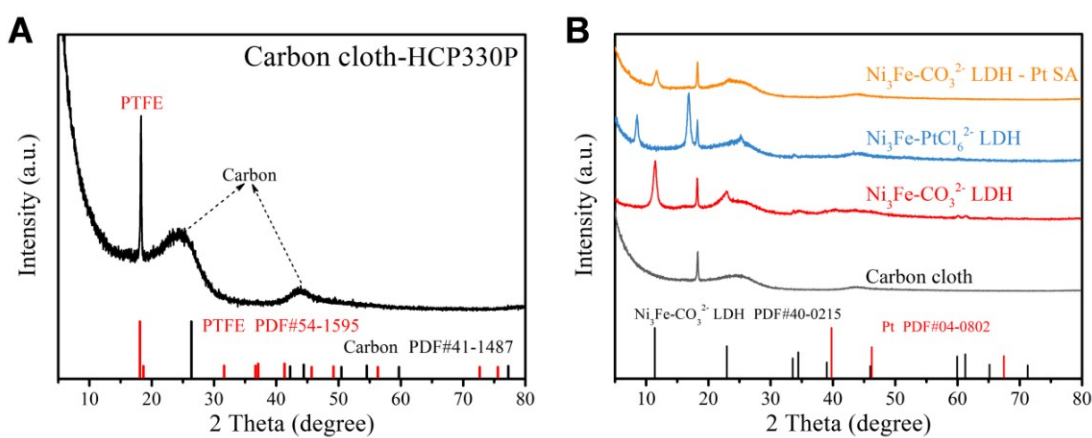


Figure S9. (A) XRD pattern of carbon cloth (HCP330P). (B) XRD patterns of $\text{Ni}_3\text{Fe-CO}_3^{2-}$ LDH, $\text{Ni}_3\text{Fe-PtCl}_6^{2-}$ LDH and $\text{Ni}_3\text{Fe-CO}_3^{2-}$ LDH-Pt SA. For the XRD pattern of carbon cloth, the sharp peak at 18.3 degree corresponds to the (100) lattice plane of PTFE, and the broad peaks at ~26 and ~44 degree corresponds to the (002) and (101) lattice planes of carbon. There is no peak at around 40 degree, which suggests that Pt nanoparticles can not be generated during the electroreduction of $\text{Ni}_3\text{Fe-PtCl}_6^{2-}$ LDH-Pt SA to $\text{Ni}_3\text{Fe-CO}_3^{2-}$ LDH-Pt SA.

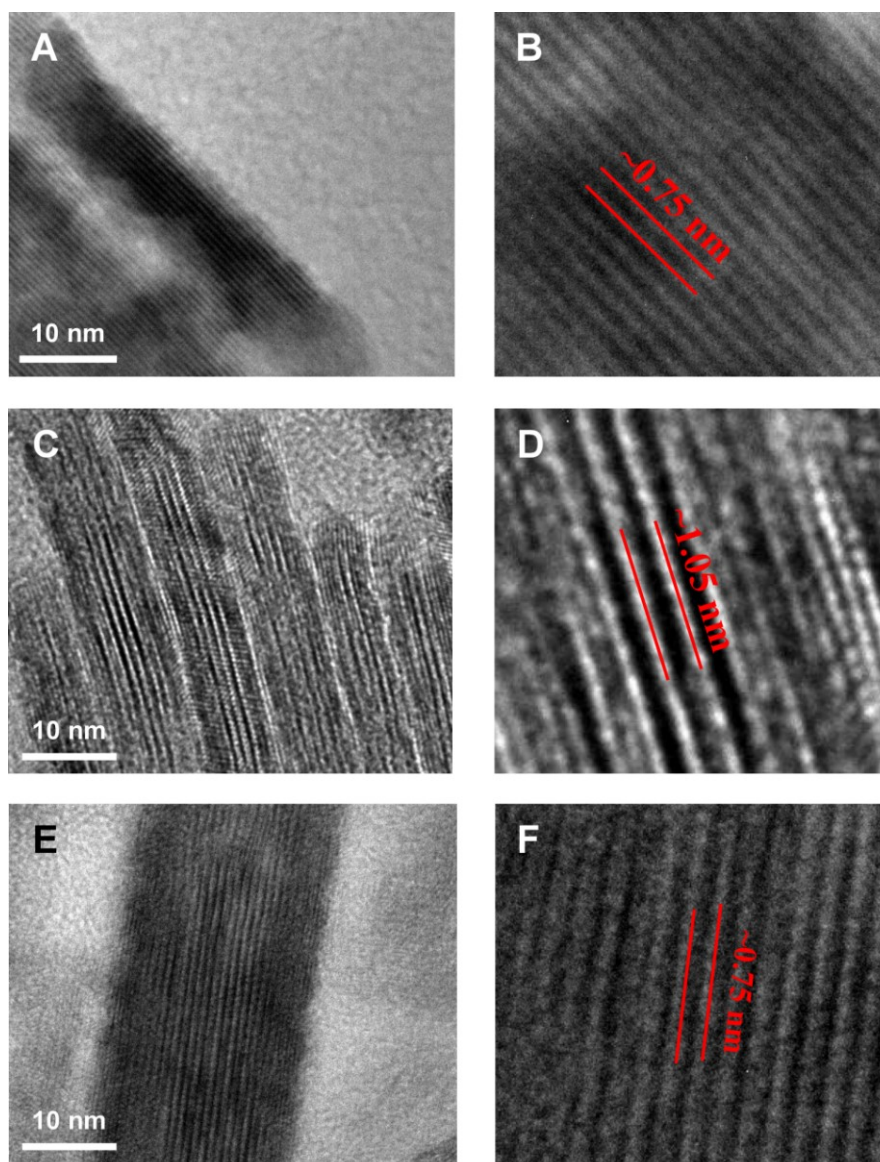


Figure S10. The cross-sectional TEM images of (A and B) $\text{Ni}_3\text{Fe-CO}_3^{2-}$ LDH, (C and D) $\text{Ni}_3\text{Fe-PtCl}_6^{2-}$ LDH and (E and F) $\text{Ni}_3\text{Fe-CO}_3^{2-}$ LDH-Pt SA nanosheets. According to the cross-sectional TEM images, the interlayer spacings of $\text{Ni}_3\text{Fe-CO}_3^{2-}$ LDH, $\text{Ni}_3\text{Fe-PtCl}_6^{2-}$ LDH and $\text{Ni}_3\text{Fe-CO}_3^{2-}$ LDH-Pt SA are ~ 0.75 , ~ 1.05 and ~ 0.75 nm, respectively.

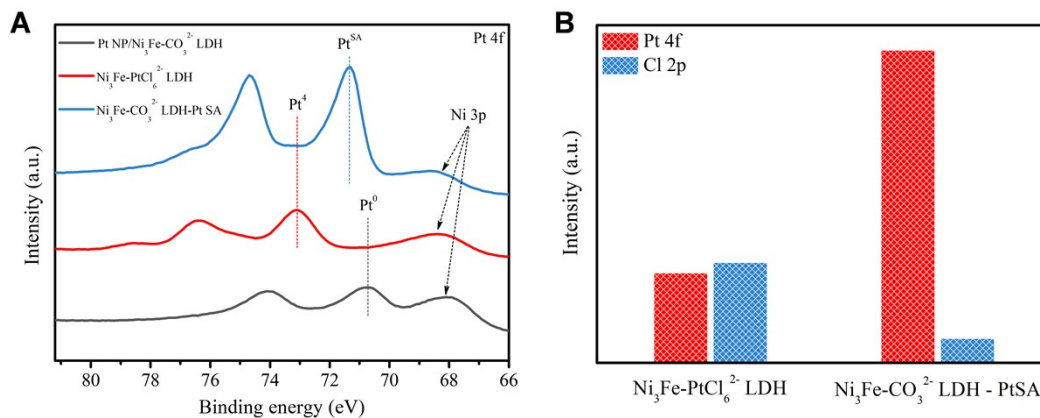


Figure S11. (A) XPS spectra for Pt 4f of Pt NP/ $\text{Ni}_3\text{Fe-CO}_3^{2-}$ LDH, $\text{Ni}_3\text{Fe-PtCl}_6^{2-}$ LDH and $\text{Ni}_3\text{Fe-CO}_3^{2-}$ LDH-Pt SA. (B) the area ratio of Pt 4f to Cl 2p for $\text{Ni}_3\text{Fe-PtCl}_6^{2-}$ LDH and $\text{Ni}_3\text{Fe-CO}_3^{2-}$ LDH-Pt SA.

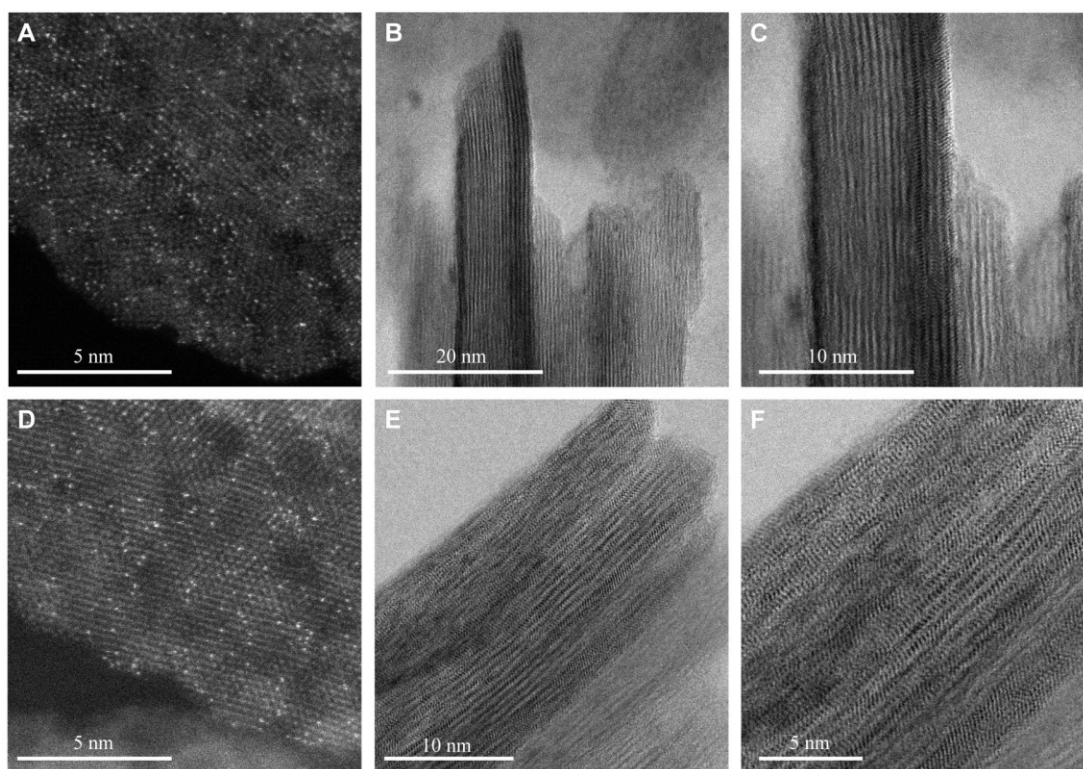


Figure S12. (A and D) HAADF-STEM images of $\text{Ni}_3\text{Fe-CO}_3^{2-}$ LDH-Pt SA nanosheets. (B, C, E and F) ABF-STEM images focusing on side-face of $\text{Ni}_3\text{Fe-CO}_3^{2-}$ LDH-Pt SA nanosheets.

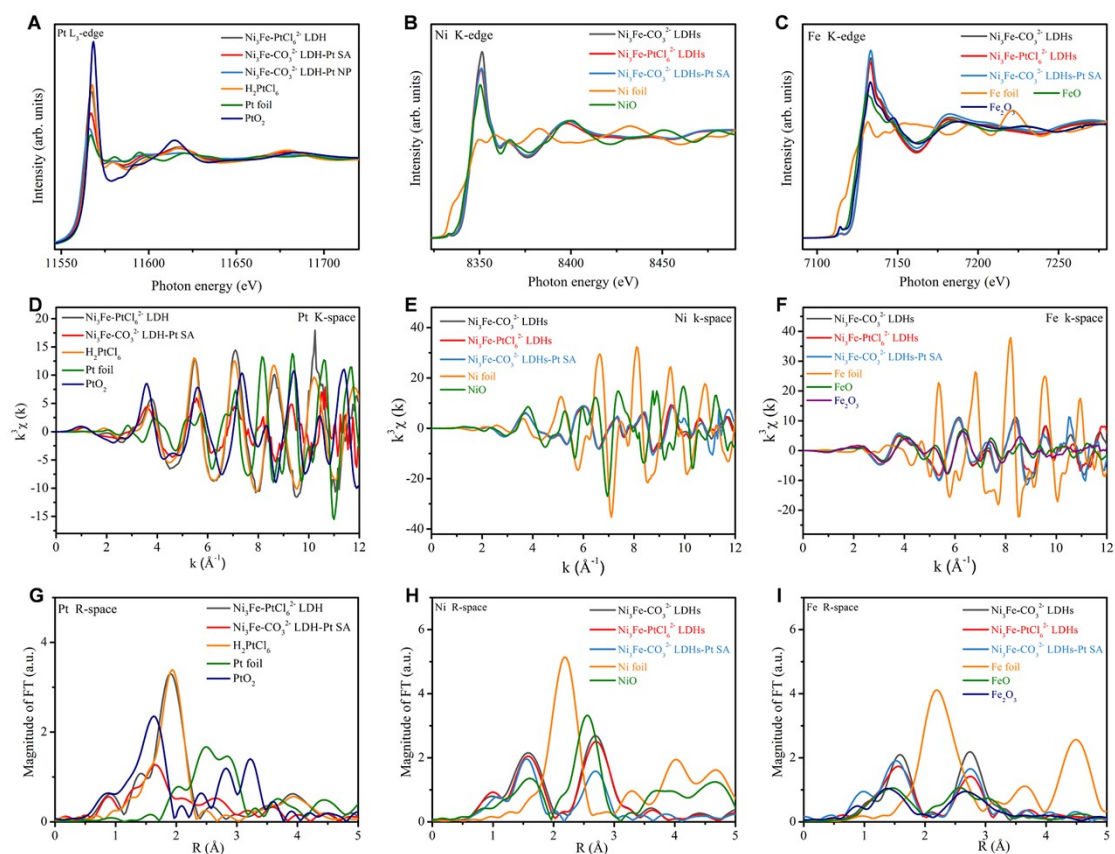


Figure S13. The normalized XANES spectra at (A) Pt L_{3} -edge, (B) Ni K-edge, and (C) Fe K-edge for $\text{Ni}_3\text{Fe-CO}_3^{2-}$ LDH, $\text{Ni}_3\text{Fe-PtCl}_6^{2-}$ LDH, $\text{Ni}_3\text{Fe-CO}_3^{2-}$ LDH-Pt SA, and standard samples. The k^3 -Weighted EXAFS spectra at (D) Pt L_{3} -edge, (E) Ni K-edge, and (F) Fe K-edge for $\text{Ni}_3\text{Fe-CO}_3^{2-}$ LDH, $\text{Ni}_3\text{Fe-PtCl}_6^{2-}$ LDH, $\text{Ni}_3\text{Fe-CO}_3^{2-}$ LDH-Pt SA, and standard samples. The k^3 -weighted Fourier transform spectra from EXAFS at (G) Pt L_{3} -edge, (H) Ni K-edge, and (I) Fe K-edge for $\text{Ni}_3\text{Fe-CO}_3^{2-}$ LDH, $\text{Ni}_3\text{Fe-PtCl}_6^{2-}$ LDH, $\text{Ni}_3\text{Fe-CO}_3^{2-}$ LDH-Pt SA, and standard samples.

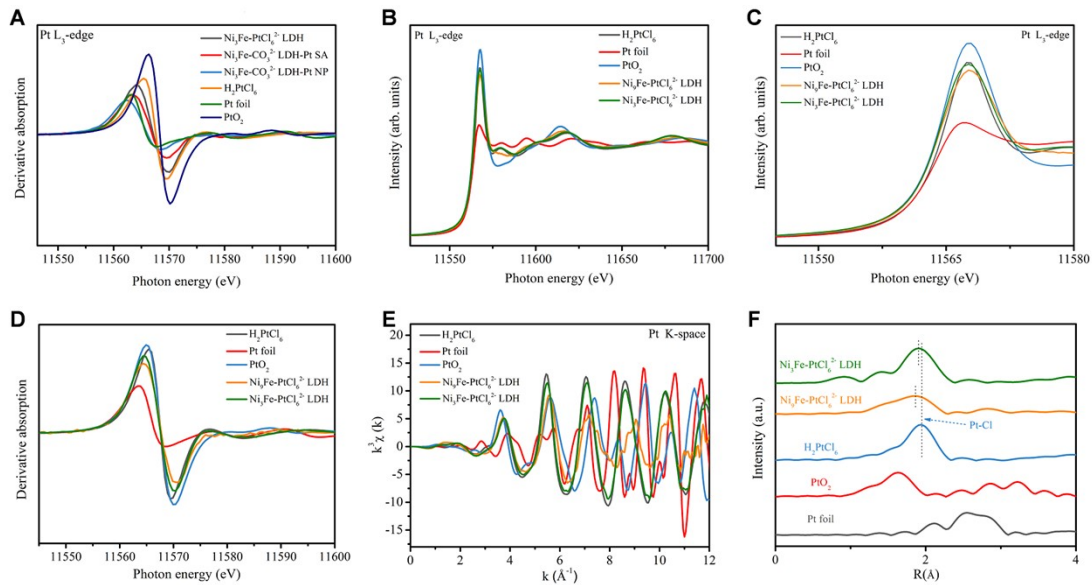


Figure S14. (A) The first derivative of the XANES spectra at Pt L₃-edge for Ni₃Fe-PtCl₆²⁻ LDH, Ni₃Fe-CO₃²⁻ LDH-Pt SA, Ni₃Fe-CO₃²⁻ LDH-Pt NP, and standard samples. (B and C) The XANES spectra at Pt L₃-edge, (D) the first derivative of the XANES spectra at Pt L₃-edge, (E) the k³-Weighted EXAFS spectra at Pt L₃-edge, and (F) FT k³χ(k)-R space curves for Pt L₃-edge of H₂PtCl₆, Pt foil, PtO₂, Ni₃Fe-PtCl₆²⁻ LDH, Ni₃Fe-PtCl₆²⁻ LDH, and standard samples. The predominant peaks for Pt L₃-edge of [Ni_{0.75}Fe_{0.25}(OH)₂]^{0.25+}(PtCl₆²⁻)_{0.125}·xH₂O and [Ni_{0.9}Fe_{0.1}(OH)₂]^{0.1+}(PtCl₆²⁻)_{0.05}·xH₂O are 1.90 Å, 1.86 Å, respectively. Based on the Pt-Cl peak around 1.94 Å in H₂PtCl₆ and Pt-O peak around 1.64 Å in PtO₂, we speculate that PtCl₆-O-Fe³⁺ results in shortening of average bond length for interlayer PtCl₆²⁻ in NiFe-PtCl₆²⁻ LDH. Compared with [Ni_{0.75}Fe_{0.25}(OH)₂]^{0.25+}(PtCl₆²⁻)_{0.125}·xH₂O, lower amount of interlayer PtCl₆²⁻ in [Ni_{0.9}Fe_{0.1}(OH)₂]^{0.1+}(PtCl₆²⁻)_{0.05}·xH₂O may lead to higher ratio of Pt-O to Pt-Cl, hence, the average bonds length of Pt in [Ni_{0.9}Fe_{0.1}(OH)₂]^{0.1+}(PtCl₆²⁻)_{0.05}·xH₂O is shorter than that of [Ni_{0.75}Fe_{0.25}(OH)₂]^{0.25+}(PtCl₆²⁻)_{0.125}·xH₂O.

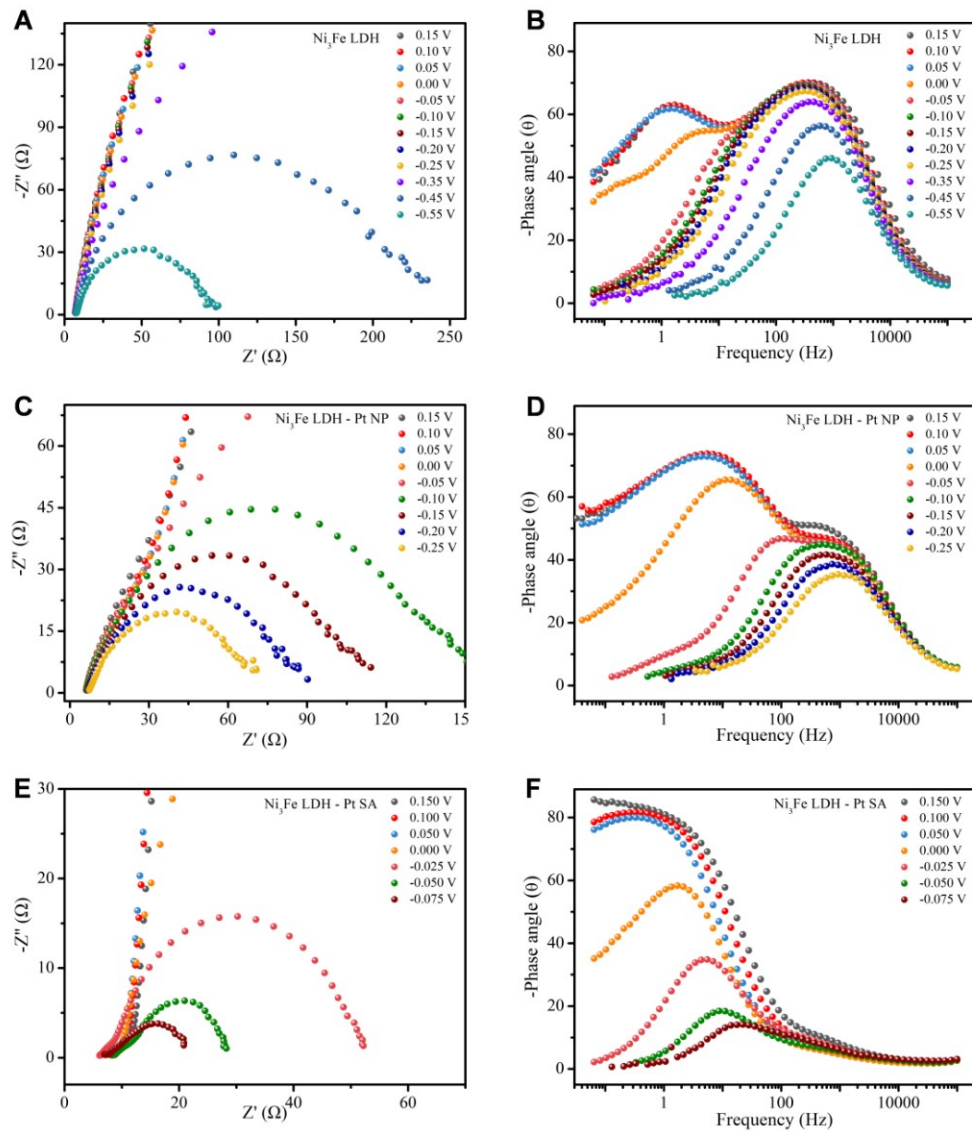


Figure S15. Nyquist and Bode plots for (A, B) $\text{Ni}_3\text{Fe-CO}_3^{2-}$ LDH, (C, D) Ni_3Fe LDH-Pt NP and (E, F) $\text{Ni}_3\text{Fe-CO}_3^{2-}$ LDH-Pt SA. Corresponding optimum fit parameters for impedance data are shown in Supplementary Tables 1-3. The high, middle and low frequency regions represent electron transfer ability, interface reaction charge transfer and reaction intermediate accumulation, respectively. For $\text{Ni}_3\text{Fe-CO}_3^{2-}$ LDH-Pt SA, the electron transfer is so fast that there is no obvious high-frequency response in its Bode plots.

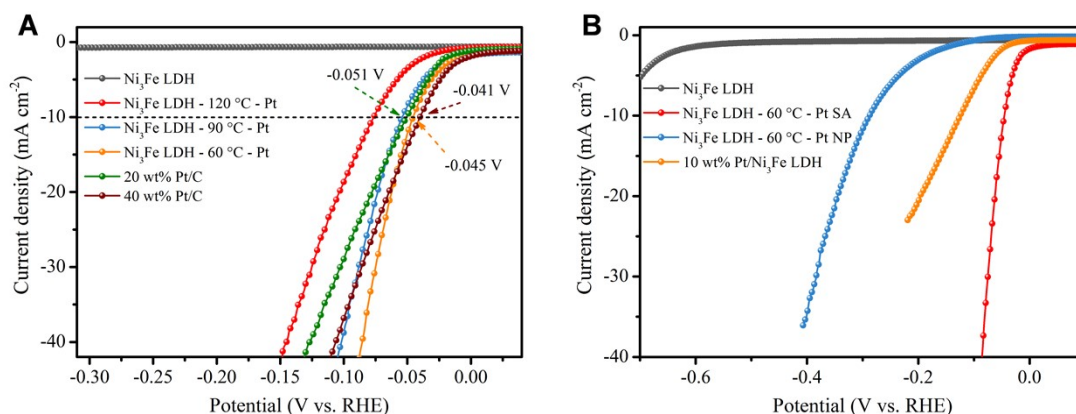


Figure S16. HER polarization curves in 1 M KOH at a scan rate of 5 mV s^{-1} for (A) Ni₃Fe LDH, Ni₃Fe LDH-120°C-Pt SA, Ni₃Fe LDH-90°C-Pt SA, Ni₃Fe LDH-60°C-Pt SA, commercial 20 wt% Pt/C and commercial 40 wt% Pt/C, (B) Ni₃Fe LDH, Ni₃Fe LDH-60°C-Pt SA, Ni₃Fe LDH-Pt NP and 10 wt% Pt NP/Ni₃Fe LDH. Ni₃Fe LDH support has terrible HER performance. As Pt single-atom increases in Ni₃Fe LDH, corresponding HER performance is greatly promoted. For Pt NP/Ni₃Fe LDH, 10 wt% Pt nanoparticles are loaded on the surface of Ni₃Fe-CO₃²⁻ LDH nanosheets; for Ni₃Fe LDH-Pt NP, most Pt nanoparticles are intercalated in the interlamination of Ni₃Fe LDH nanosheets. Compared with Pt NP/Ni₃Fe LDH, Ni₃Fe LDH-Pt NP shows poor HER performance, which indicates that interlayer Pt nanoparticles, intercalated in the interlamination of LDH, can not display HER performance as well as it should. For Ni₃Fe-PtCl₆²⁻ LDH, there must also be some PtCl₆²⁻ anions adsorbed on the surface of LDH; therefore, for Ni₃Fe-CO₃²⁻ LDH-Pt SA, there are Pt single atoms on the surface and the inside of LDH. Hence, we hold the opinion that, for Ni₃Fe-CO₃²⁻ LDH-Pt SA, interlayer Pt single-atom promotes the electron transfer ability of Ni₃Fe LDH support, and Pt single-atom shows excellent HER performance on the surface of LDH nanosheets.

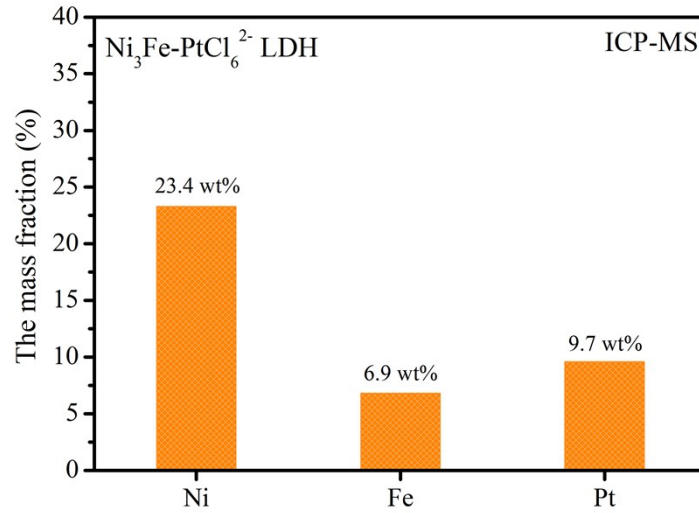


Figure S17. Inductively coupled plasma-mass spectrometry for Ni₃Fe LDH-60°C-Pt SA.

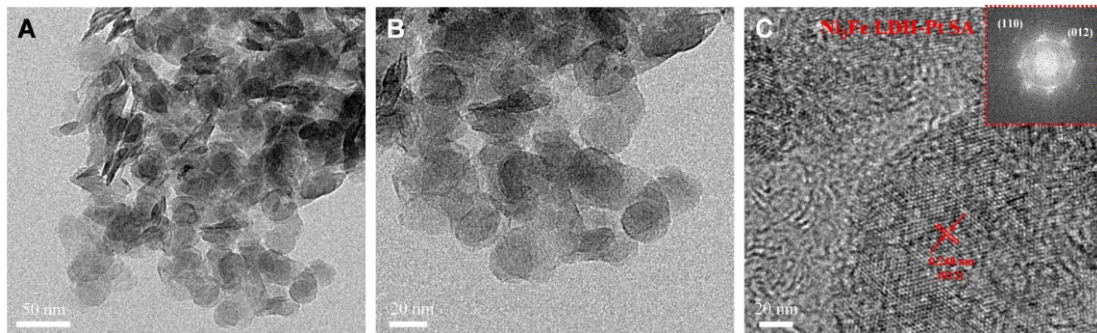


Figure S18. TEM images of Ni₃Fe-CO₃²⁻ LDH-Pt SA after long-term HER test. The lattice spacings are found to be 0.25 nm corresponding to the distance of (012) lattice plane of Ni₃Fe-CO₃²⁻ LDH-Pt SA.

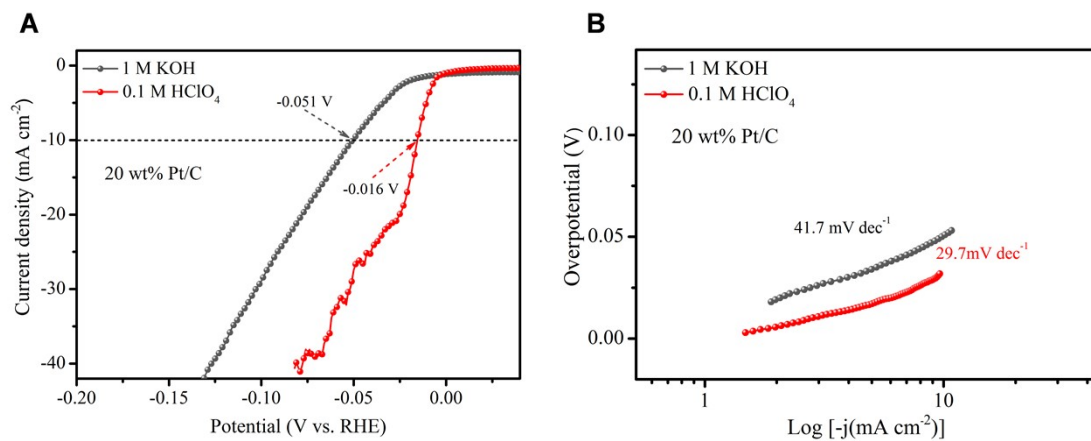


Figure S19. A, HER polarization curves for 20 wt% Pt/C in 1 M KOH and 0.1 HClO₄ at a scan rate of 5 mV s⁻¹.

B, Corresponding Tafel slopes.

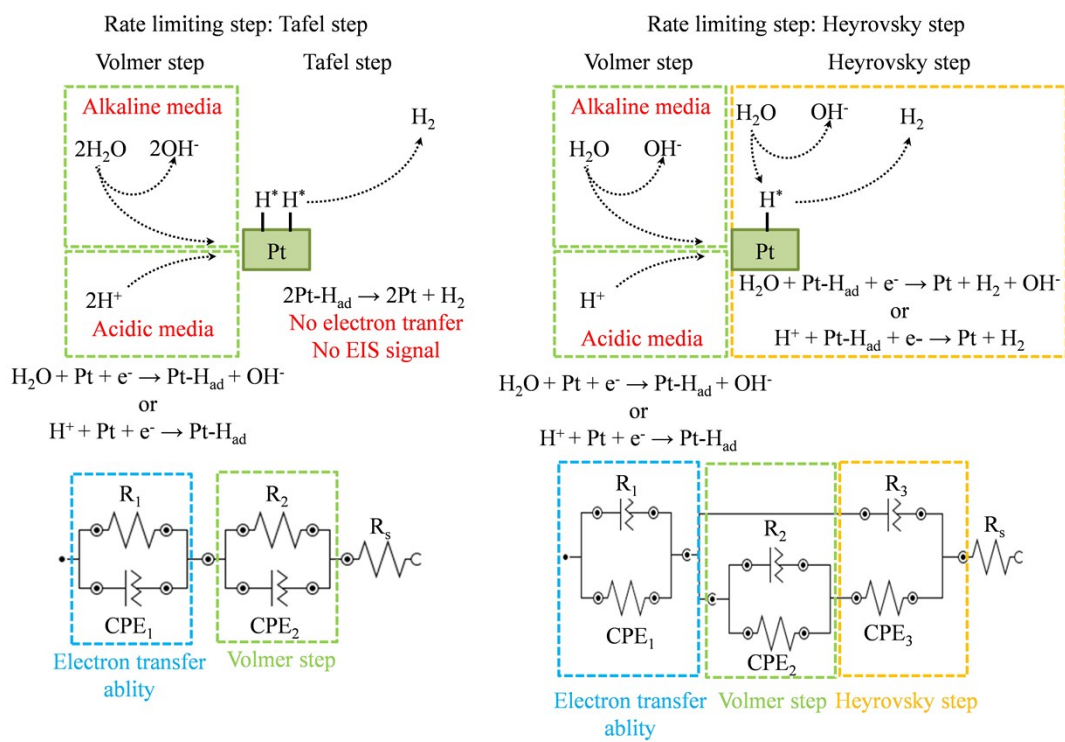


Figure S20. Schematic diagram of HER mechanism and corresponding equivalent circuit for Pt/C. In theory, with Tafel step as RDS, Volmer step with electron transfer can be identified by EIS; however, Tafel step cannot be identified because of without electron transfer. With Heyrovsky step as RDS, Volmer and Heyrovsky steps with electron transfer can be identified by EIS.

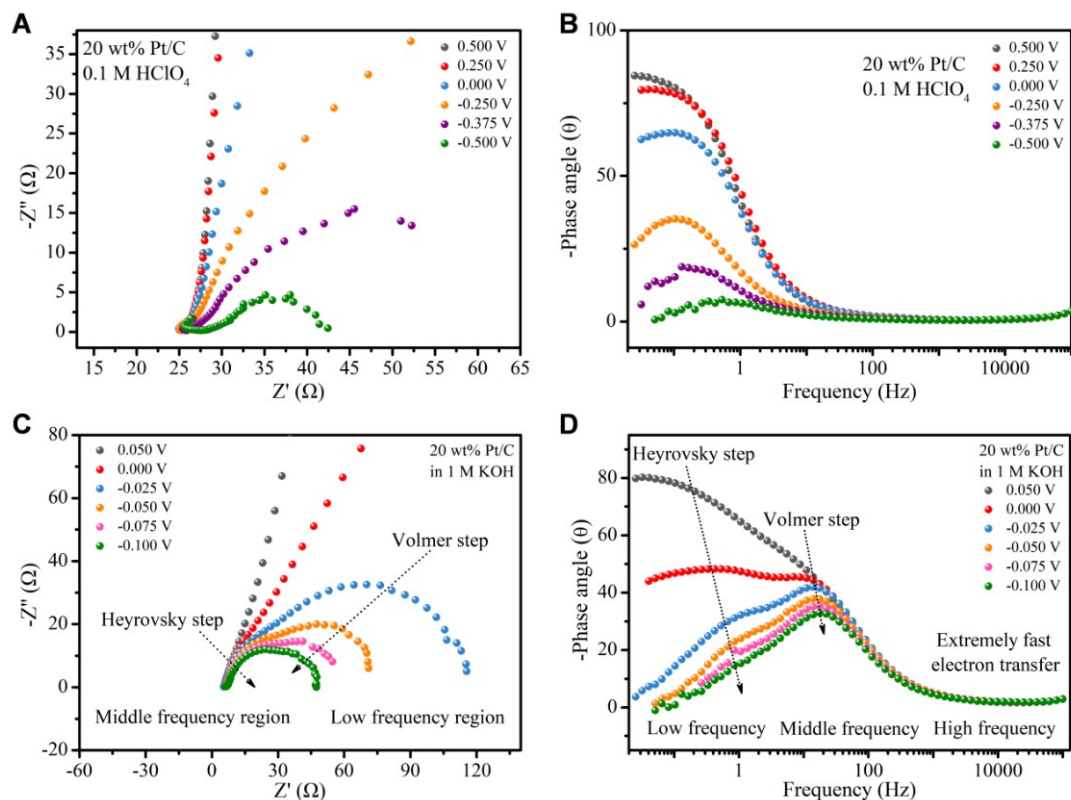


Figure S21. Nyquist and Bode plots for 20 wt% Pt/C in (A, B) 0.1 HClO₄ and (C, D) 1 M KOH. Corresponding optimum fit parameters for impedance data are shown in Supplementary Tables 4-6. Peaks at low and middle frequency regions represent Volmer and Heyrovsky steps, respectively. In acidic media (0.1 HClO₄), only one peak appears at low frequency region according with theoretic HER mechanism with Tafel step as RDS. However, in alkaline media (1 M KOH), two peaks appear at low and middle frequency regions, respectively, which conforms to Heyrovsky-Volmer mechanism with Heyrovsky step as RDS.

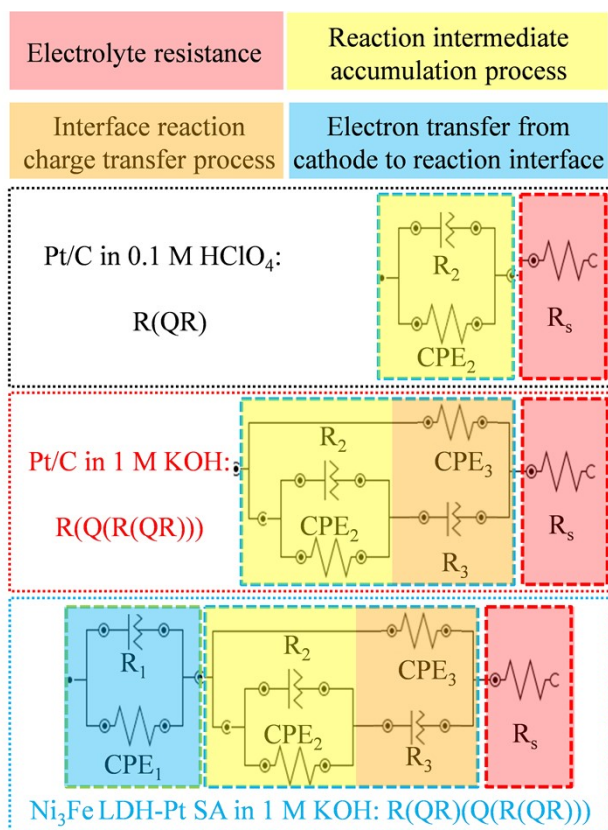


Figure S22. The equivalent circuits for HER of Pt/C in 0.1 HClO₄ or 1 M KOH media and Ni₃Fe LDH-Pt SA in 1 M KOH. The signals at the high frequency and low frequency regions can be ascribed to the electronic conduction of catalyst inner-layer/catalyst surface-layer interface and the reaction charge transfer on the electrolyte/catalyst interface, respectively. Based on HER mechanism, we used the equivalent circuit model, which consists of four parts: (1) The first section of parallel circuit containing resistance (R_1) and constant phase element (CPE_1) is corresponding to the electron transfer from cathode (catalyst inner-layer) to reaction interface; (2) The second section of parallel circuit containing resistance (R_2) and constant phase element (CPE_2) responds to the reaction intermediate (H_{ad}) accumulation; (3) The third section of parallel circuit containing resistance (R_3) and constant phase element (CPE_3) is corresponding to interface reaction charge transfer (the electrochemical desorption of H_{ad}); (4) R_s is interpreted as electrolyte resistance (Fig. 3A). Owing to excellent electron transfer ability of Pt/C, CPE_1 & R_1 can be ignored in the equivalent circuits. In 0.1 HClO₄ of Pt/C, CPE_3 & R_3 can be ignored because of Tafel-Volmer mechanism (Fig. S20, ES†).

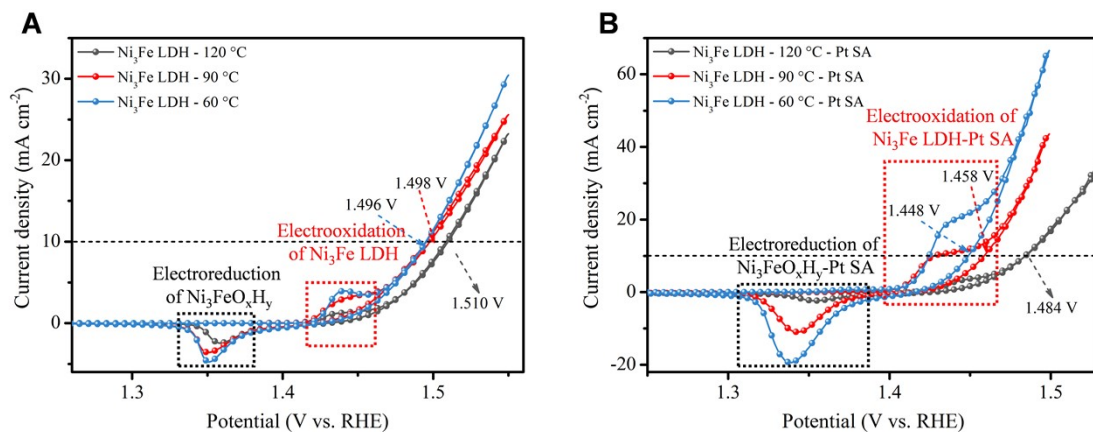


Figure S23. OER polarization curves for (A) Ni₃Fe LDH-120 °C, Ni₃Fe LDH-90 °C and Ni₃Fe LDH-60 °C and (B) Ni₃Fe LDH-120 °C-Pt SA, Ni₃Fe LDH-90 °C-Pt SA and Ni₃Fe LDH-60 °C-Pt SA at scan of 5 mV⁻¹. At forward scan for OER polarization curves, electrooxidation of Ni₃Fe LDH or Ni₃Fe LDH-Pt SA occurs before OER. At backward scan for OER polarization curves, electroreduction of Ni₃FeO_xH_y or Ni₃FeO_xH_y-Pt SA occurs.

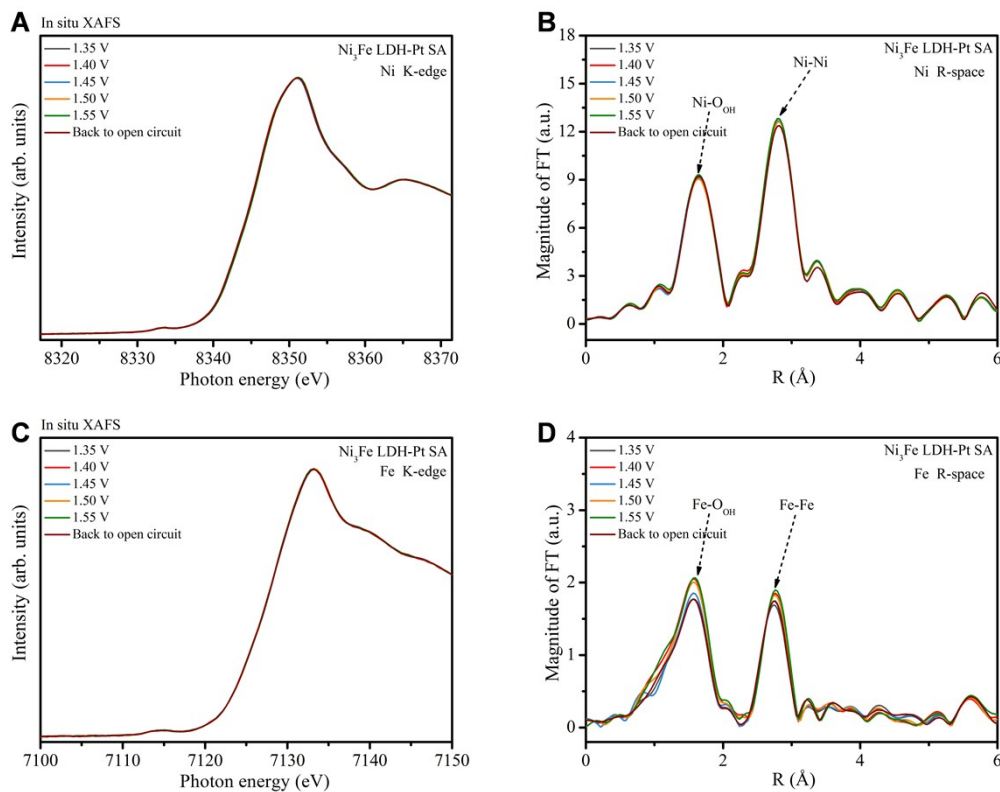


Figure S24. In situ (A) XANES spectra and (B) FT $k^3\chi(k)$ -R space curves at Ni K-edge for Ni₃Fe-CO₃²⁻ LDH-Pt SA. In situ (C) XANES spectra and (D) FT $k^3\chi(k)$ -R space curves at Fe K-edge for Ni₃Fe-CO₃²⁻ LDH-Pt SA.

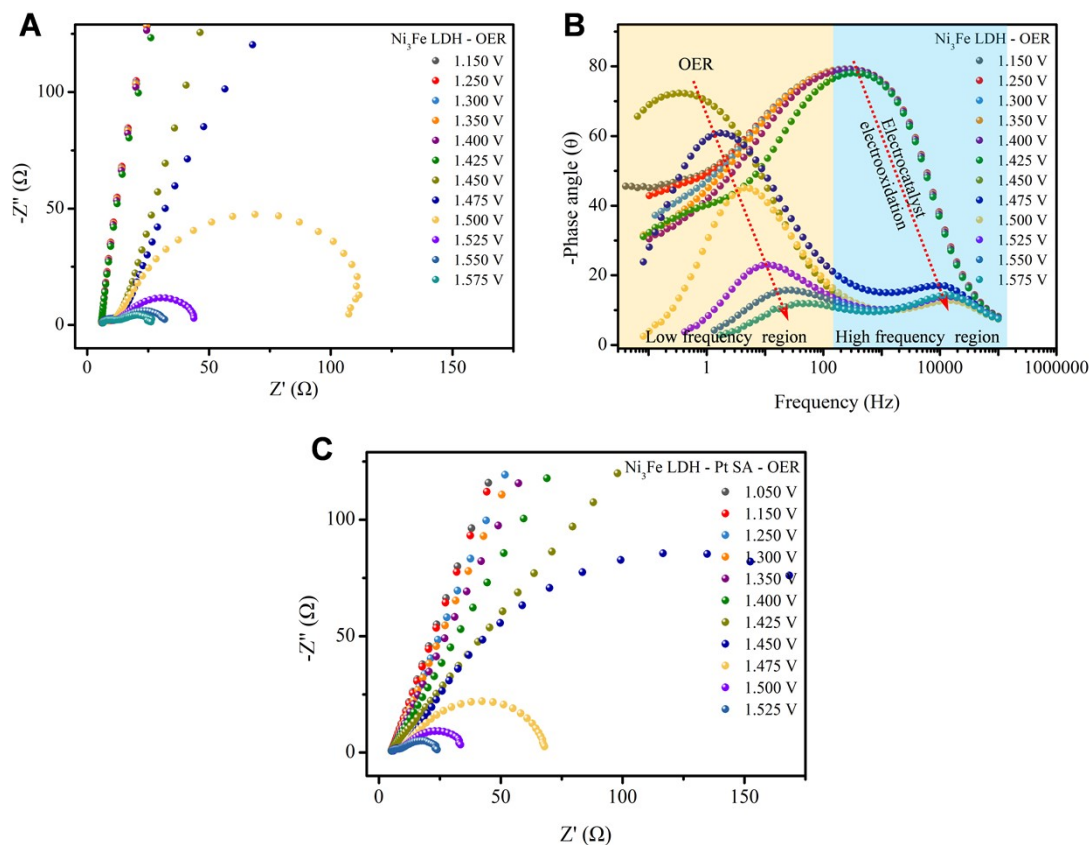


Figure S25. EIS Nyquist and Bode plots for (A, B) Ni_3Fe LDH and (C) Ni_3Fe LDH-Pt SA during OER in 1 M KOH. The Bode plots for $\text{Ni}_3\text{Fe-CO}_3^{2-}$ LDH-Pt SA during OER are shown in Fig. 5D. Before electrocatalyst electrooxidation reaction for both $\text{Ni}_3\text{Fe-CO}_3^{2-}$ LDH and $\text{Ni}_3\text{Fe-CO}_3^{2-}$ LDH-Pt SA (1.05 to 1.40 V), theoretically, only original electrocatalyst/diffuse double layer (DDL) interface at high frequency region with extremely weak charge transfer exists according to R(QR) model. During electrocatalyst electrooxidation reaction without OER (1.425 to 1.450 V), combining with in situ Raman spectra, the high frequency interface reaction with ultrafast charge transfer occurs according to swift electrocatalyst electrooxidation reaction, meanwhile, low frequency interface with extremely weak charge transfer appears representing sluggish OER, which proves that low frequency interface between oxide layer ($\text{Ni}_3^{2+\delta}\text{FeO}_x\text{H}_y$ or $\text{Ni}_3^{2+\delta}\text{FeO}_x\text{H}_y\text{-Pt SA}$) and DDL is formed by electrocatalyst electrooxidation. During drastic OER process (1.450 to 1.525 V), the progressively reduced -Phase angle of low frequency region consists with the current density of OER, which proves that, the OER active site is directly related to the electrogenerated oxide layer and OER occurs at low frequency interface (oxide layer/DDL).

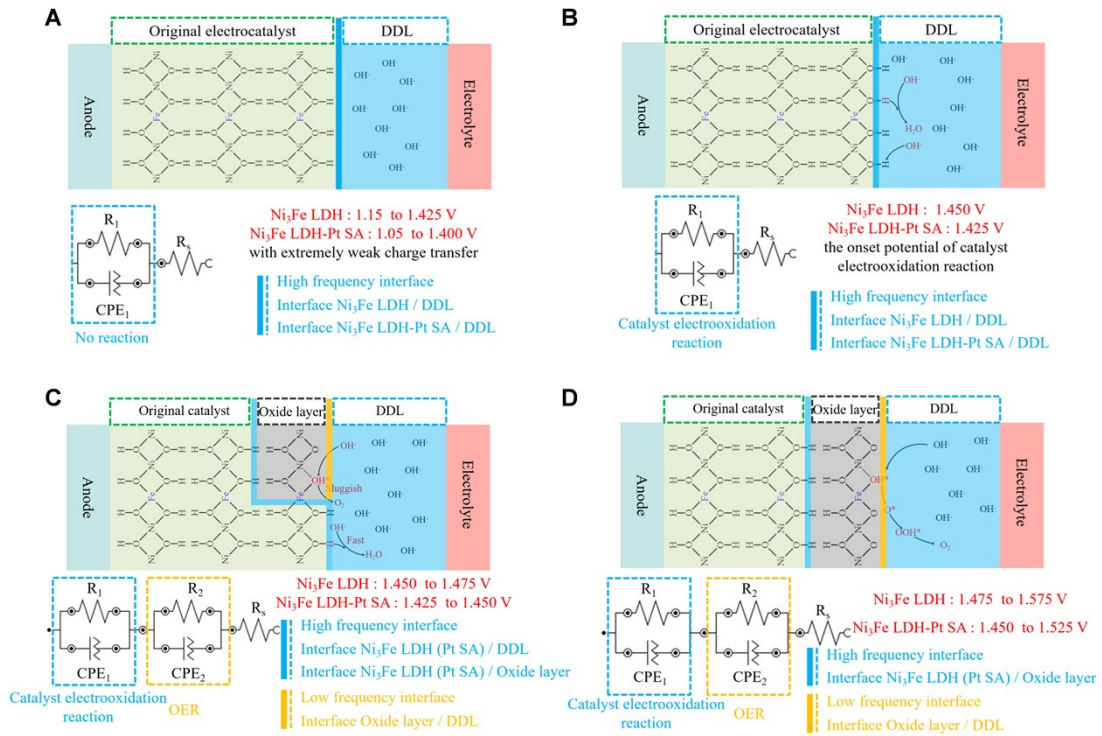


Figure S26. Two equivalent circuit models for OER of $Ni_3Fe-CO_3^{2-}$ LDH and $Ni_3Fe-CO_3^{2-}$ LDH-Pt SA at different potentials. In the equivalent circuit models, CPE_1R_1 loop and CPE_2R_2 loop of equivalent circuit models represent the dielectric property and resistivity of the interface reaction with electron transfer at the high frequency interface and the low frequency interface, respectively. The R_s represents the electrolyte resistance. The high frequency interface represents the interface between the original electrocatalyst (NiFe LDH or NiFe LDH-Pt SA) and DDL. The low frequency interface represents the interface between the oxide layer and DDL. The oxide layer is considered as the interface where OER takes place.

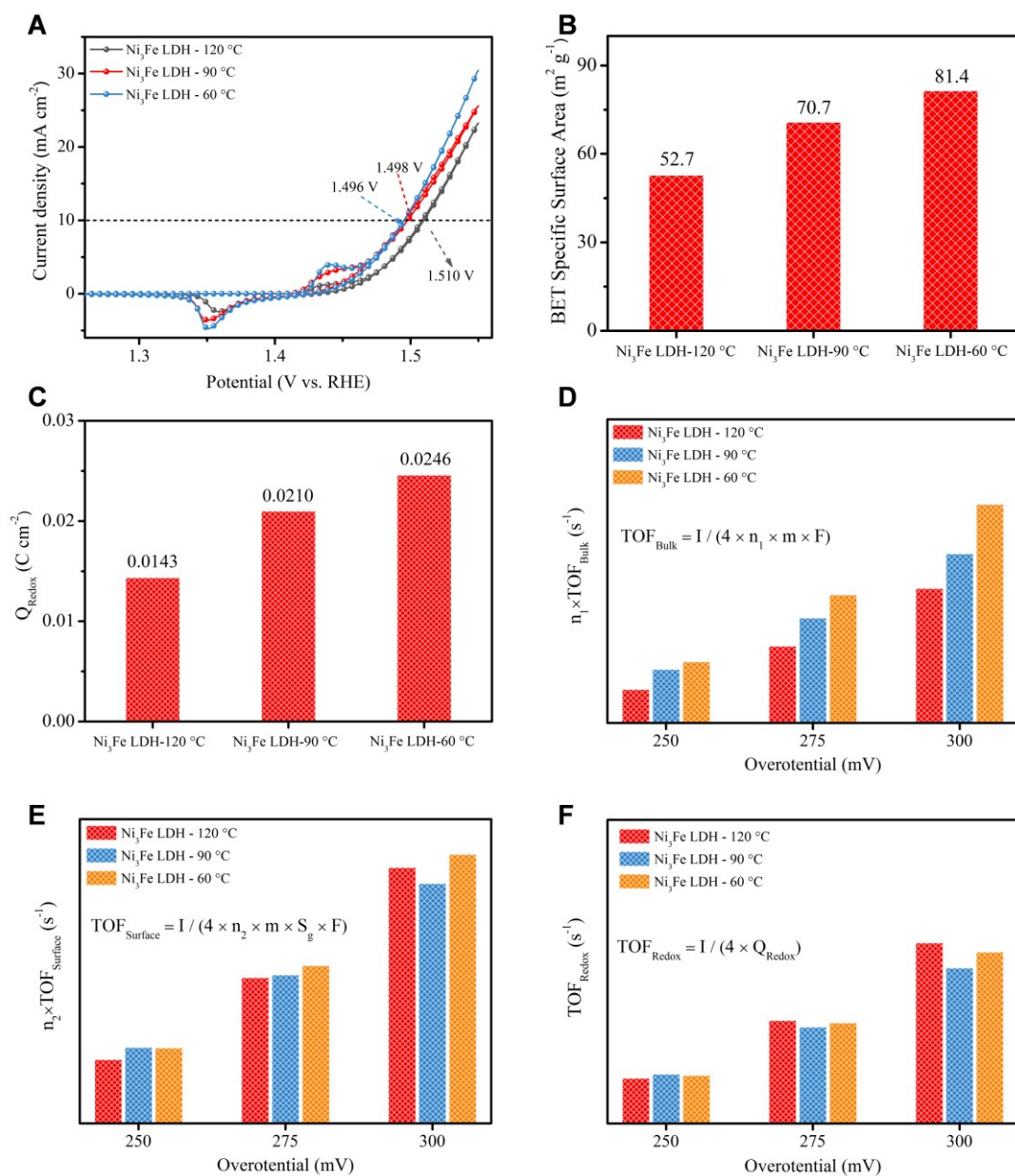


Figure S27. (A) OER polarization curves, (B) BET specific surface areas, (C) electron transfer number of redox ($\text{Ni}^{2+}/\text{Ni}^{3+}$), (D) TOF_{Bulk} , (E) $\text{TOF}_{\text{Surface}}$ and (F) $\text{TOF}_{\text{Redox}}$ for $\text{Ni}_3\text{Fe}-\text{CO}_3^{2-}$ LDH with different size and thickness synthesized in different temperature. Smaller size and thinner thickness of $\text{Ni}_3\text{Fe}-\text{CO}_3^{2-}$ LDH lead to an increase in BET specific surface area, meanwhile, the numbers of transfer electron of $\text{Ni}^{2+}/\text{Ni}^{3+}$ redox for $\text{Ni}_3\text{Fe}-\text{CO}_3^{2-}$ LDH with different sizes and thickness during OER are obtained from redox peak, which provides basis to calculate TOF_{bulk} , $\text{TOF}_{\text{surface}}$ and $\text{TOF}_{\text{redox}}$.

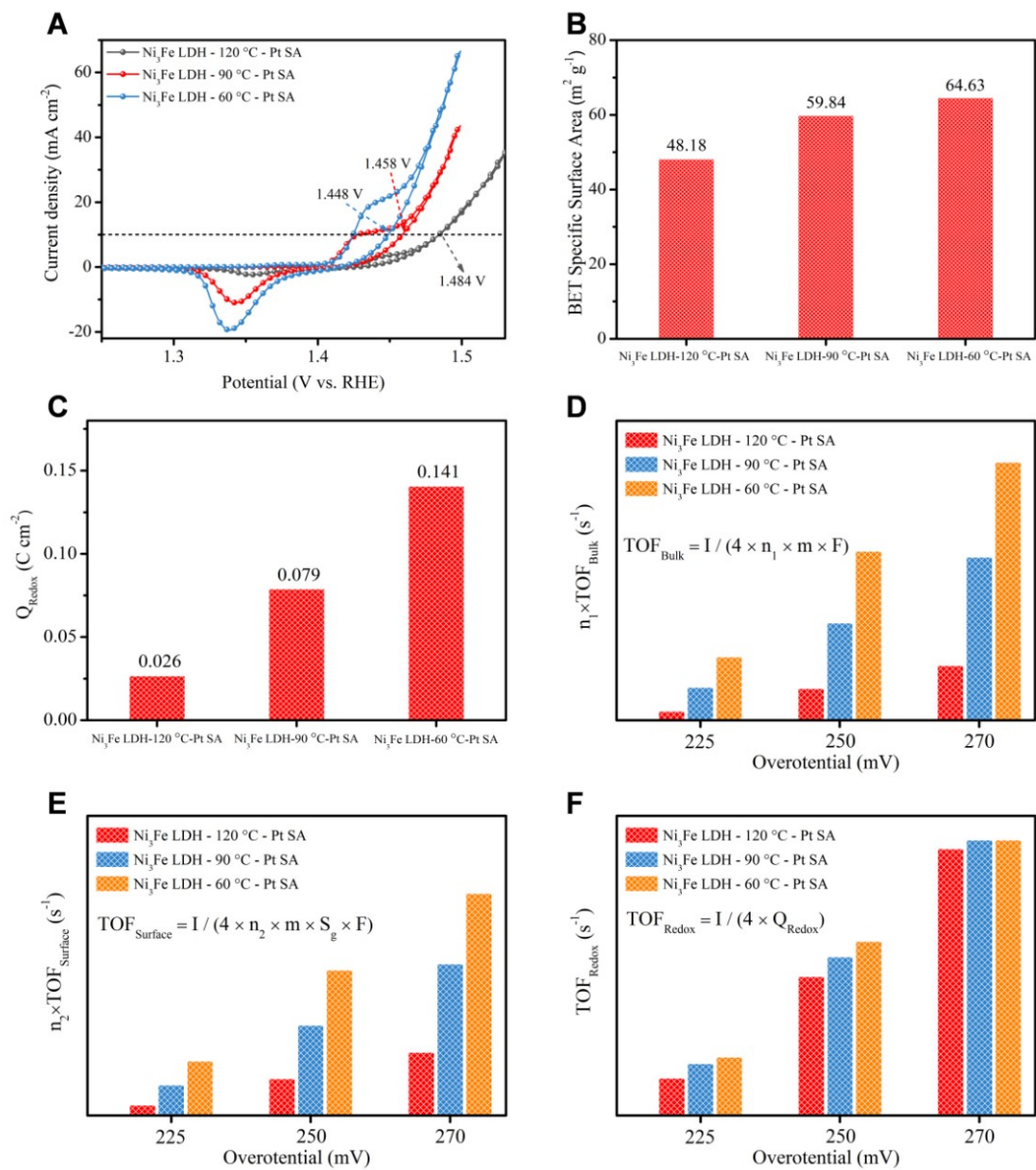


Figure S28. (A) OER polarization curves, (B) BET specific surface areas, (C) electron transfer number of redox (Ni²⁺/Ni³⁺), (D) TOF_{Bulk}, (E) TOF_{Surface} and (F) TOF_{Redox} for Ni₃Fe-CO₃²⁻ LDH-Pt SA with different size, thickness and Pt single-atom loading.

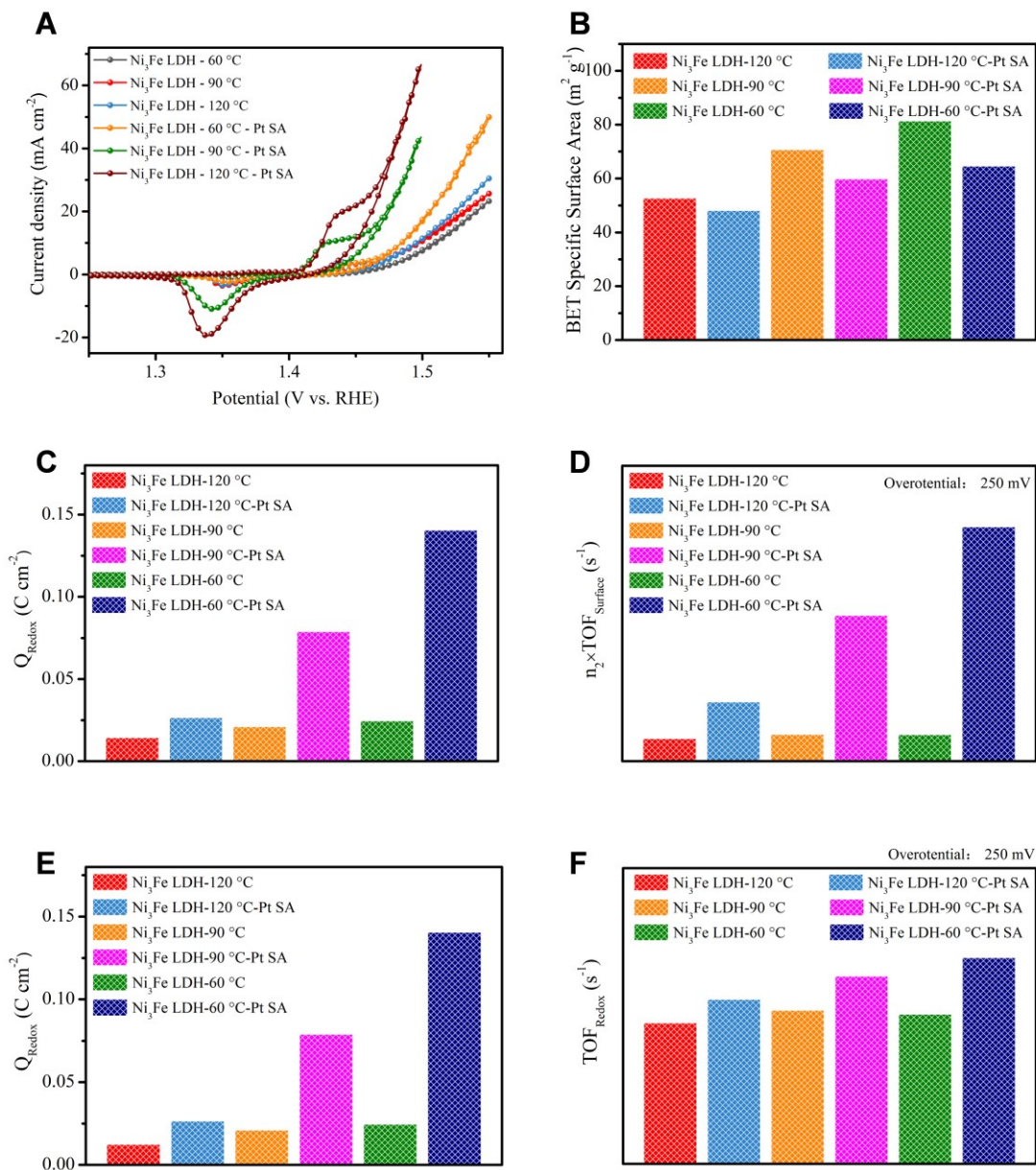


Figure S29. (A) OER polarization curves, (B) BET specific surface areas, (C) electron transfer number of redox ($\text{Ni}^{2+}/\text{Ni}^{3+}$), (D) TOF_{Bulk} , (E) $\text{TOF}_{\text{Surface}}$ and (F) $\text{TOF}_{\text{Redox}}$ for $\text{Ni}_3\text{Fe-CO}_3^{2-}$ LDH and corresponding $\text{Ni}_3\text{Fe-CO}_3^{2-}$ LDH-Pt SA.

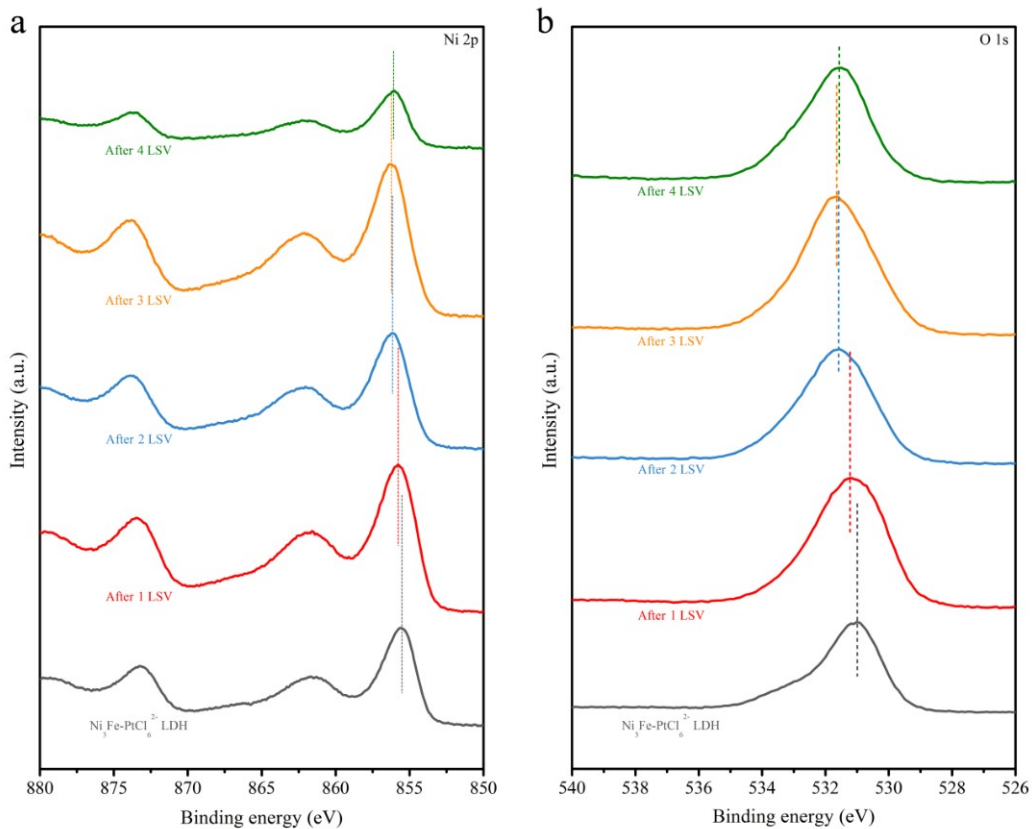


Figure S30. XPS spectra of Ni 2p in $\text{Ni}_3\text{Fe-PtCl}_6^{2-}$ LDH after different numbers cycles LSV. Cycles LSV curves are shown in Fig. 2A.

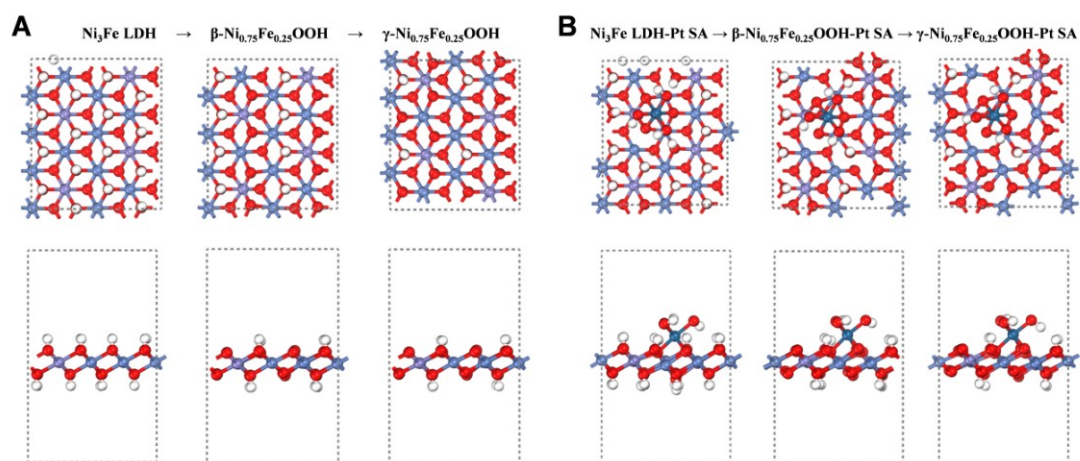


Figure S31. Electrocatalysts electrooxidation reactions for $\text{Ni}_3\text{Fe-CO}_3^{2-}$ LDH and $\text{Ni}_3\text{Fe-CO}_3^{2-}$ LDH-Pt SA. For $\text{Ni}_3\text{Fe-CO}_3^{2-}$ LDH and $\text{Ni}_3\text{Fe-CO}_3^{2-}$ LDH-Pt SA, active phase transitions are from $\text{Ni}_3\text{Fe-CO}_3^{2-}$ LDH to $\gamma\text{-Ni}_{0.75}\text{Fe}_{0.25}\text{OOH}$ and from $\text{Ni}_3\text{Fe-CO}_3^{2-}$ LDH-Pt SA to $\gamma\text{-Ni}_{0.75}\text{Fe}_{0.25}\text{OOH-Pt SA}$, respectively.

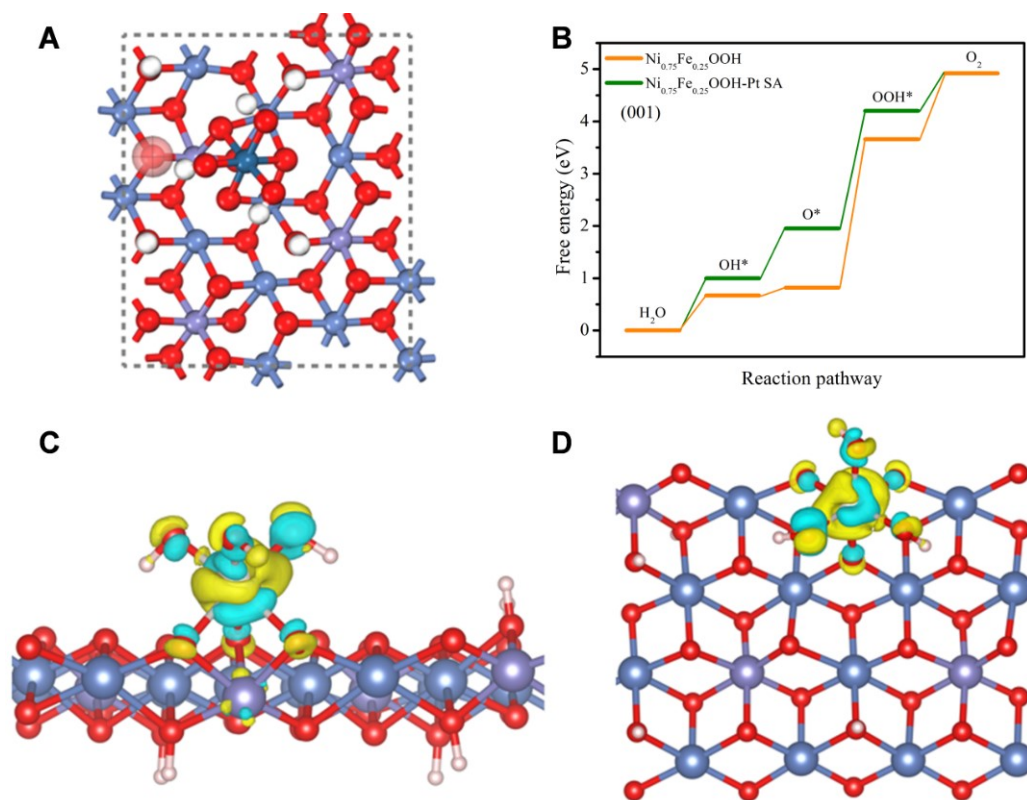


Figure S32. A, Single-layer slab model for $\gamma\text{-Ni}_{0.75}\text{Fe}_{0.25}\text{OOH-Pt SA}$ at (001) plane. B, Free energy diagram for the OER of $\gamma\text{-Ni}_{0.75}\text{Fe}_{0.25}\text{OOH-Pt SA}$ at (001) plane ($\text{Ni}^{3+5}\text{-O-Fe}^{3+6}$). C-D, (C) Side and (D) front differential charge densities of $\gamma\text{-Ni}_{0.75}\text{Fe}_{0.25}\text{OOH-Pt SA}$ at (100) plane.

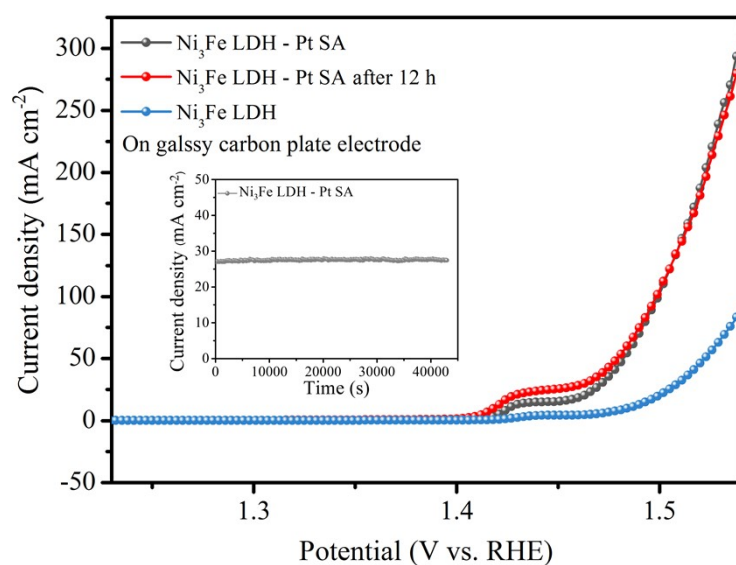


Figure S33. Stability test for $\text{Ni}_3\text{Fe-CO}_3^{2-}$ LDH-Pt SA carried out on glassy carbon plate electrode (1cm^2), keeping the same testing condition as glassy carbon electrode (0.196cm^2).

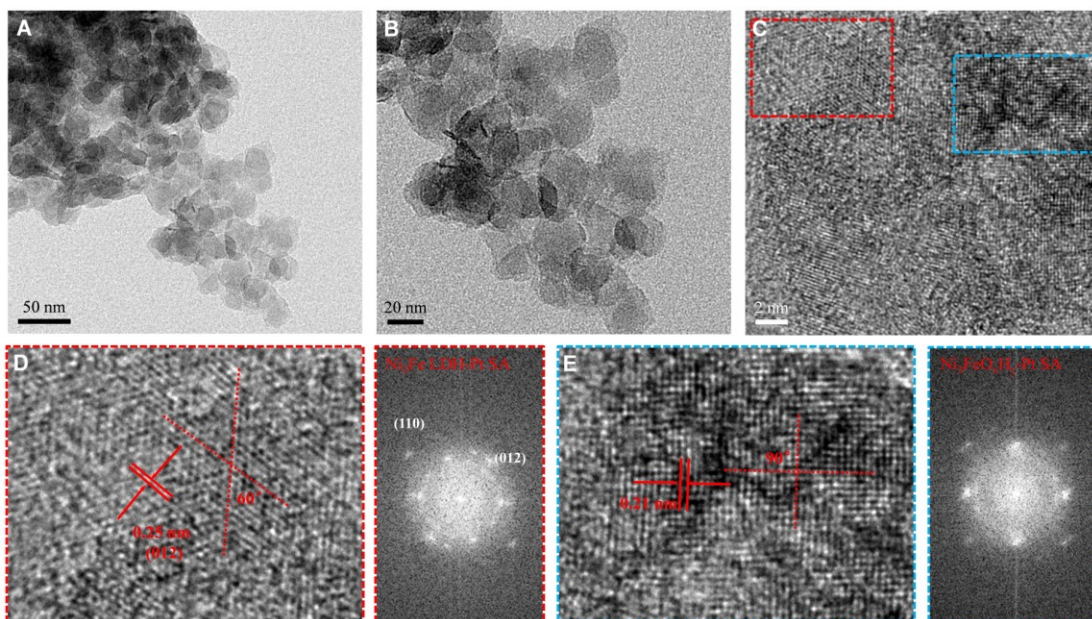


Figure S34. (A, B and C) TEM images, (D and E) partial enlarged drawing and corresponding electronic diffraction patterns of $\text{Ni}_3\text{Fe-CO}_3^{2-}$ LDH-Pt SA after long-term OER test.

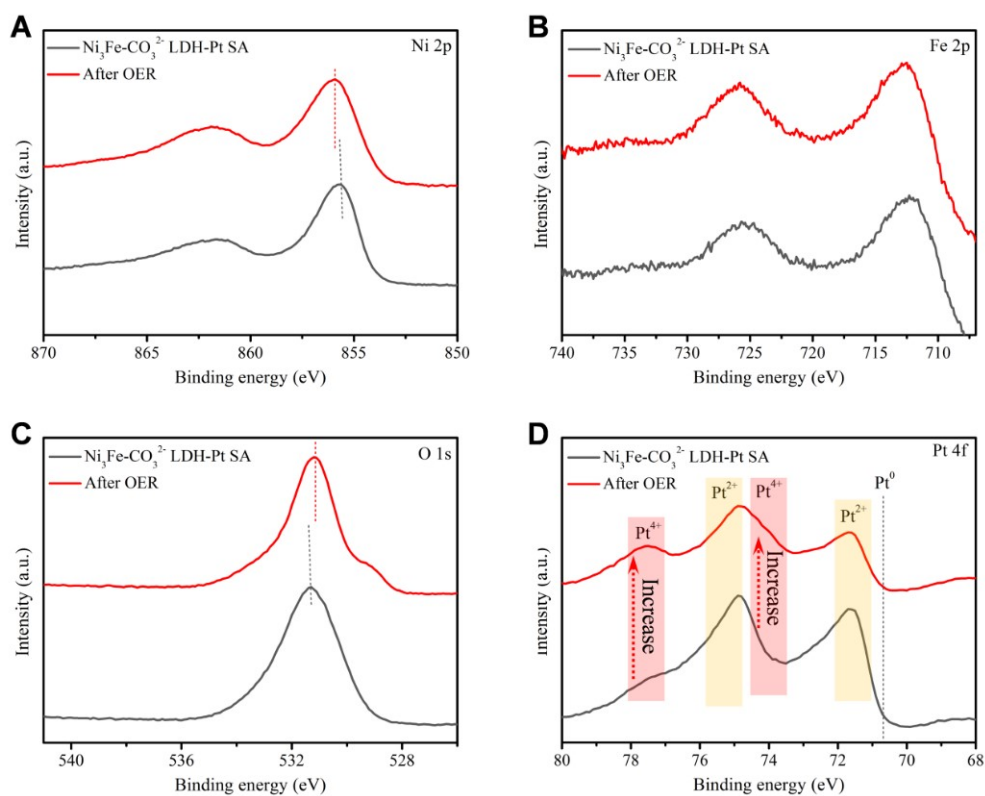


Figure S35. XPS spectra for (A) Ni 2p, (B) Fe 2p, (C) O 1s and (D) Pt 4f of $\text{Ni}_3\text{Fe-CO}_3^{2-}$ LDH-Pt SA and $\text{Ni}_3\text{Fe-CO}_3^{2-}$ LDH-Pt SA after OER.

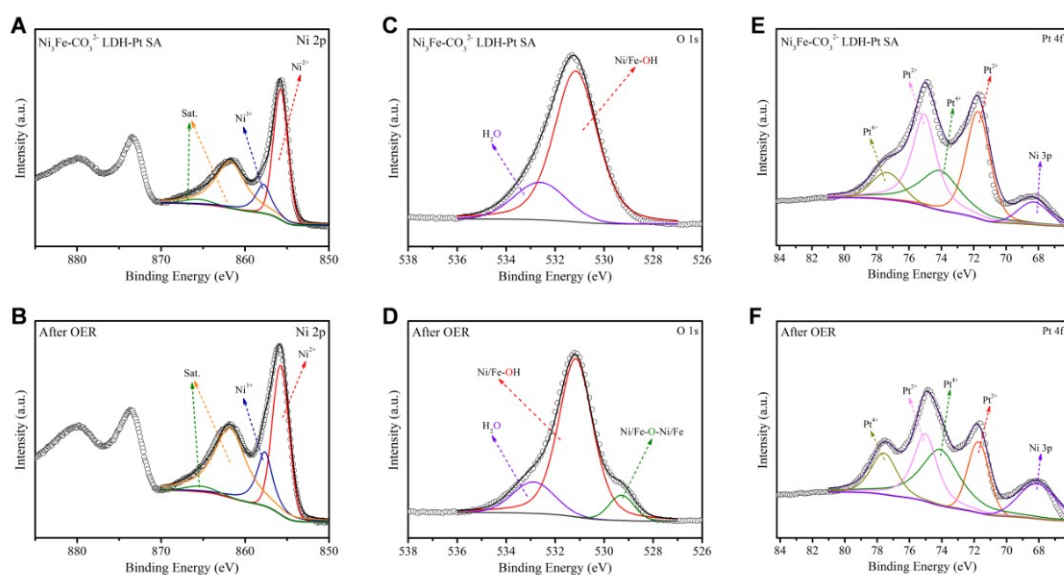


Figure S36. XPS spectra: (A, B) Ni 2p, (C, D) O 1s and (E, F) Pt 4f of $\text{Ni}_3\text{Fe-CO}_3^{2-}$ LDH-Pt SA and $\text{Ni}_3\text{Fe-CO}_3^{2-}$ LDH-Pt SA after OER. The Ni 2p XPS spectra are fitted using four components: a peak at 855.80 eV corresponding to Ni^{2+} , peak at 857.70 eV corresponding to Ni^{3+} and two satellite peaks. The O 1s XPS spectra are fitted using three components: a peak at 532.90 eV corresponding to adsorbed H_2O , two peaks at 531.10 eV and 529.30 eV corresponding to M-OH and M-O, respectively. The Pt 4f XPS spectra are fitted using five components: a peak at 68.0 eV corresponding to Ni 3p, two peaks at 71.70 eV and 75.05 eV corresponding to Pt^{2+} , and two peaks at 74.30 eV and 77.65 eV corresponding to Pt^{4+} .

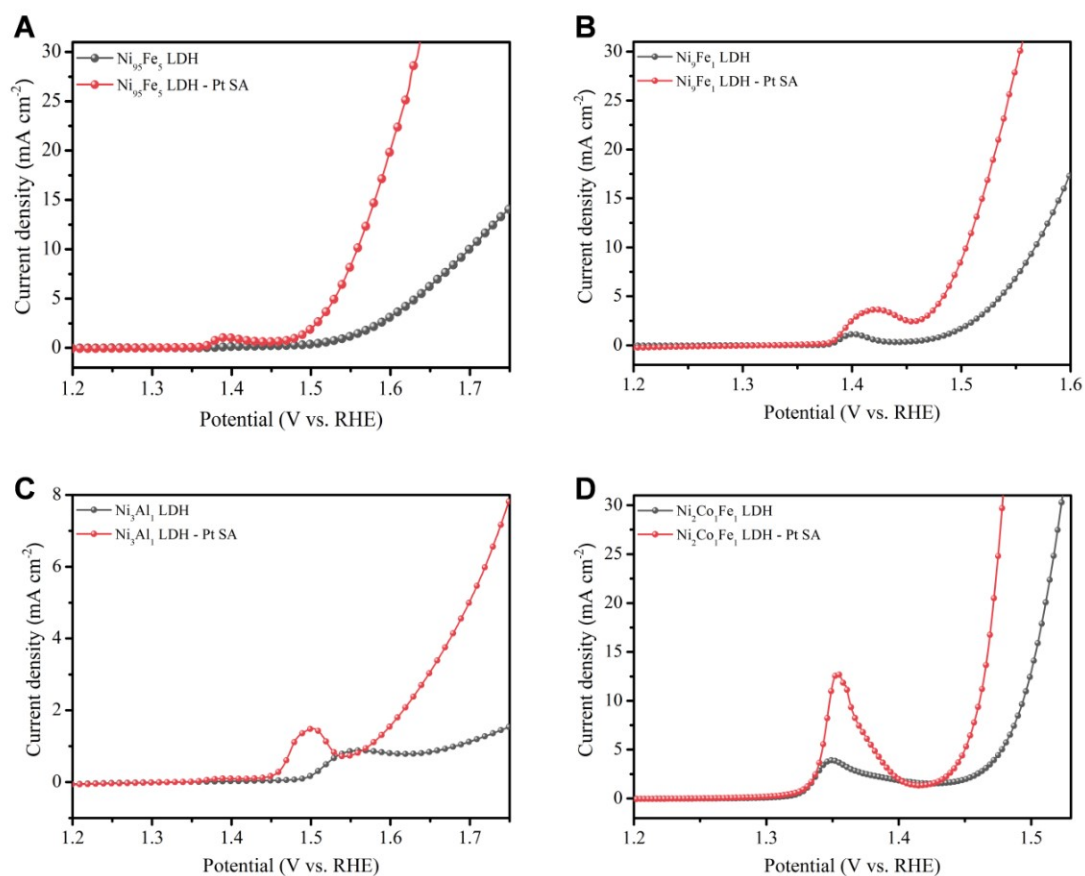


Figure S37. OER polarization curves for (A) Ni₉₅Fe₅-CO₃²⁻ LDH and Ni₉₅Fe₅-CO₃²⁻ LDH-Pt SA, (B) Ni₉Fe₁-CO₃²⁻ LDH and Ni₉Fe₁-CO₃²⁻ LDH-Pt SA, (C) Ni₃Al₁-CO₃²⁻ LDH and Ni₃Al₁-CO₃²⁻ LDH-Pt SA and (D) Ni₂Co₁Fe₁-CO₃²⁻ LDH and Ni₂Co₁Fe₁-CO₃²⁻ LDH-Pt SA.

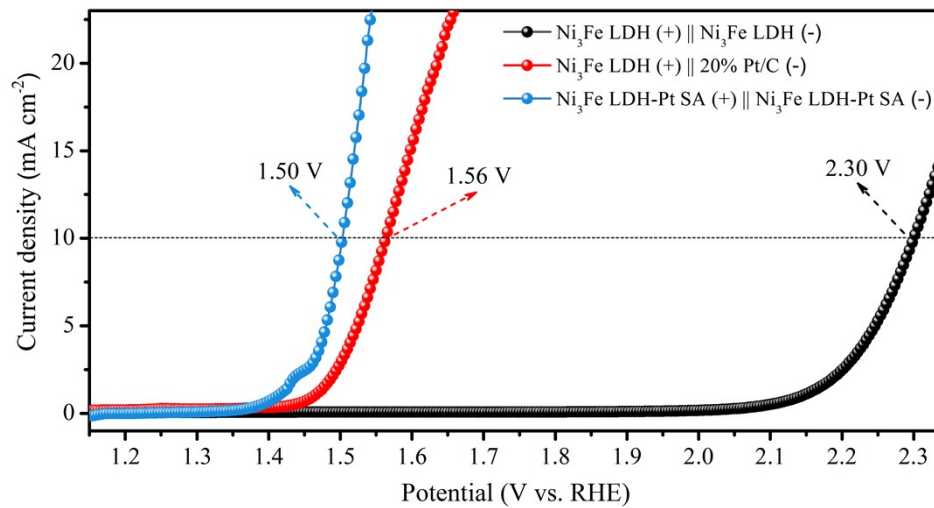


Figure S38. Polarization curve for overall water splitting with the Ni₃Fe-CO₃²⁻ LDH-Pt SA electrode as both the anode and cathode at a scan rate of 5 mV s⁻¹.

Supporting Tables

Table S1. Optimum fit parameters for the impedance date of Ni₃Fe-CO₃²⁻ LDH during HER in 1 M KOH.

E V vs. RHE	R _s Ω	Q ₁ μS s ⁿ cm ⁻²	n ₁	R ₁ Ω	Q ₂ μS s ⁿ cm ⁻²	n ₂	R ₂ Ω	Q ₃ μS s ⁿ cm ⁻²	n ₃	R ₃ Ω
0.10	7.00	26.1	0.86	3618	26.1	0.86	490.7	40.0	0.80	180300
0.05	7.00	17.5	0.80	2900	15.9	0.88	761.5	64.7	0.71	50060
0.00	6.95	65.7	0.75	3479	16.6	0.90	571.1	17.6	0.79	17000
-0.05	7.19	49.4	0.62	2357	18.3	0.74	331.7	13.5	0.90	762.7
-0.10	6.62	52.2	0.61	1876	65.1	0.85	126.4	13.4	0.47	481.1
-0.15	7.21	61.9	0.73	1484	66.7	0.71	7.21	14.4	0.90	341.3
-0.20	7.18	17.3	0.89	1087	26.0	0.74	4.37	11.2	0.96	361.7
-0.25	7.11	17.7	0.88	637.1	22.3	0.96	0.08	20.1	0.96	340.4
-0.35	7.07	49.5	0.83	423.2	27.4	0.53	0.09	34.2	0.91	128.8
-0.45	7.28	74.9	0.86	159.8	20.4	0.78	0.06	163.0	0.98	46.11
-0.55	7.71	154.0	0.75	47.63	12.1	0.80	0.01	277.0	0.91	39.26

Table S2. Optimum fit parameters for the impedance date of Ni₃Fe LDH-Pt NP during HER in 1 M KOH.

E V vs. RHE	R _s Ω	Q ₁ μS s ⁿ cm ⁻²	n ₁	R ₁ Ω	Q ₂ μS s ⁿ cm ⁻²	n ₂	R ₂ Ω	Q ₃ μS s ⁿ cm ⁻²	n ₃	R ₃ Ω
0.10	5.94	8.76	0.77	3314	68.2	0.90	8996	4.9	0.88	13140
0.05	5.92	3.02	0.83	571	88.9	0.78	56.35	10.8	0.85	23710
0.00	5.93	1.95	0.83	314.1	57.7	0.79	32.56	9.7	0.81	3095
-0.05	5.97	70.80	0.86	210.1	79.0	0.80	22.36	15.6	0.87	33.75
-0.10	5.82	86.80	0.76	94.37	78.6	1.00	19.38	10.4	0.88	48.56
-0.15	6.72	70.40	0.78	93.85	128.0	0.78	9.20	10.7	0.85	19.79
-0.20	6.91	65.40	0.76	58.03	8980	0.70	4.97	29.7	0.99	14.26
-0.25	7.22	12.20	0.89	41.47	6930	0.91	4.24	63.2	0.77	12.75

Table S3. Optimum fit parameters for the impedance date of Ni₃Fe-CO₃²⁻ LDH-Pt SA during HER in 1 M KOH.

E V vs. RHE	R _s Ω	Q ₁ μS s ⁿ cm ⁻²	n ₁	R ₁ Ω	Q ₂ μS s ⁿ cm ⁻²	n ₂	R ₂ Ω	Q ₃ μS s ⁿ cm ⁻²	n ₃	R ₃ Ω
0.050	8.22	2009	0.52	3.35	1799	0.94	6750	688	0.96	1090
0.000	8.02	1702	0.56	3.20	2365	0.92	263.1	2989	0.87	74.0
-0.025	6.11	1914	0.61	2.76	3147	0.85	40.17	2998	0.85	6.89
-0.050	8.13	2393	0.59	2.67	2659	0.92	13.94	3802	0.88	4.97
-0.075	6.84	2228	0.63	2.38	2546	0.91	7.73	2876	0.90	4.36

Table S4. Optimum fit parameters for the impedance date of 20 wt% Pt/C during HER in 0.1 HClO₄.

E V vs. RHE	R_s Ω	Q₂ μS sⁿ cm⁻²	n₂	R₂ Ω	C₂ μF cm⁻²	τ₂
0.0500	25.83	6470	0.96	130800	8474.74	1108.50
0.0250	25.77	5757	0.94	12210	7391.34	90.25
0.0000	25.61	7825	0.87	1918	11804.88	22.64
-0.0250	25.53	22530	0.75	173.7	35616.68	6.19
-0.0375	26.07	31410	0.65	54.19	41674.19	2.26
-0.0500	27.77	35200	0.52	17.38	22262.22	0.39

Table S5. Optimum fit parameters for the impedance date of 20 wt% Pt/C during HER in in 1 M KOH.

E V vs. RHE	R_s Ω	Q₂ μS sⁿ cm⁻²	n₂	R₂ Ω	C₂ μF cm⁻²	τ₂	Q₃ μS sⁿ cm⁻²	n₃	R₃ Ω	C₃ μF cm⁻²	τ₃
0.050	5.47	2206	0.94	29640	14802	438.73	1819	0.84	73.02	1230.90	0.0899
0.000	5.40	4483	0.60	1373	15209	20.88	1988	0.80	47.41	1093.39	0.0518
-0.020	5.46	7504	0.83	63.0	6411	0.40	1851	0.80	47.91	1007.81	0.0483
-0.050	5.48	8873	1.00	23.08	8873	0.20	1831	0.78	45.48	905.31	0.0412
-0.075	5.48	12190	1.00	13.49	12190	0.16	1615	0.81	37.02	820.51	0.0304
-0.100	5.97	20070	1.00	7.73	20070	0.15	1696	0.80	33.66	813.13	0.0274

Table S6. Optimum fit parameters for the impedance date of Ni₃Fe-CO₃²⁻ LDH-Pt SA during HER in 1 M KOH.

E V vs. RHE	C₁ μF cm⁻²	τ₁	C₂ μF cm⁻²	τ₂	C₃ μF cm⁻²	τ₃
0.050	20.17	0.000068	2120.59	14.3140	680.69	0.7419
0.000	26.98	0.000086	2269.16	0.5970	2399.01	0.1775
-0.025	66.98	0.000185	2204.10	0.0885	1505.21	0.0104
-0.050	71.42	0.000191	2024.63	0.0282	2173.33	0.0108
-0.075	102.63	0.000244	1715.82	0.0133	1720.79	0.0075

Table S7. Optimum fit parameters for the impedance date of Ni₃Fe-CO₃²⁻ LDH during OER in 1 M KOH.

E V vs. RHE	R_s Ω	Q₁ μS sⁿ cm⁻²	n₁	R₁ Ω	Q₂ μS sⁿ cm⁻²	n₂	R₂ Ω
1.15	5.044	17.05	0.8192	51370			
1.25	5.19	14.37	0.8419	32460			
1.3	5.265	13.34	0.853	24810			
1.35	5.421	11.15	0.8775	14640			
1.4	5.466	10.6	0.8858	9759			
1.425	5.521	10.54	0.9295	2262	1631	0.8254	16320
1.45	3.829	234.7	0.3828	10.97	1511	0.8447	11190
1.475	4.286	129.7	0.456	12.47	1227	0.816	884.1
1.5	4.784	552.1	0.5358	6.885	1816	0.7651	149.5
1.525	5.308	198.9	0.6245	7.057	2658	0.68	38.07
1.55	5.531	89.87	0.6984	6.661	2322	0.6695	21.4
1.575	6.045	44.97	0.759	6.136	2670	0.5955	16.29

Table S8. Optimum fit parameters for the impedance date of Ni₃Fe-CO₃²⁻ LDH-Pt SA during OER in 1 M KOH.

E V vs. RHE	R_s Ω	Q₁ μS sⁿ cm⁻²	n₁	R₁ Ω	Q₂ μS sⁿ cm⁻²	n₂	R₂ Ω
1.150	4.82	65.89	0.77	11710			
1.250	4.70	77.18	0.76	95570			
1.300	4.92	87.93	0.75	96020			
1.350	4.88	110.2	0.73	10630			
1.400	4.75	191.1	0.68	11900			
1.425	4.07	584.0	0.57	552.5	1456	0.85	3709
1.450	3.29	1017	0.29	20.68	1548	0.84	212.8
1.475	4.15	3076	0.41	9.26	1316	0.82	56.66
1.500	4.92	4271	0.58	5.20	1369	0.76	27.17
1.525	4.81	1618	0.69	4.31	1415	0.73	14.92

Table S9. TOF_{Bulk}, TOF_{Surface} and TOF_{Redox} of Ni₃Fe-CO₃²⁻ LDH.

	Ni ₃ Fe LDH-120 °C			Ni ₃ Fe LDH-90 °C			Ni ₃ Fe LDH-60 °C		
SSA/m ² g ⁻¹	52.74			70.73			81.41		
Q _{Redox} /C cm ⁻²	0.0143			0.0210			0.0246		
η/mV	250	275	300	250	275	300	250	275	300
N ₁ × TOF _{Bulk} /g ⁻¹ s ⁻¹ (×N _A)	0.0443	0.101	0.177	0.0706	0.138	0.223	0.0807	0.169	0.288
N ₂ × TOF _{Surface} /m ⁻² s ⁻¹ (×N _A)	8.40 × 10 ⁻⁴	1.92 × 10 ⁻³	3.37 × 10 ⁻³	9.99 × 10 ⁻⁴	1.95 × 10 ⁻³	3.16 × 10 ⁻³	9.91 × 10 ⁻⁴	2.08 × 10 ⁻³	3.54 × 10 ⁻³
TOF _{Redox} /s ⁻¹	59.61	135.73	238.05	64.91	127.04	205.17	63.33	132.67	226.04

Table S10. TOF_{Bulk}, TOF_{Surface} and TOF_{Redox} of Ni₃Fe-CO₃²⁻ LDH-Pt SA.

	Ni ₃ Fe LDH-120 °C-Pt SA			Ni ₃ Fe LDH-90 °C-Pt SA			Ni ₃ Fe LDH-60 °C-Pt SA		
SSA/m ² g ⁻¹	48.18			59.84			64.63		
Q _{Redox} /C cm ⁻²	0.026			0.079			0.141		
η/mV	225	250	270	225	250	270	225	250	270
N ₁ × TOF _{Bulk} /g ⁻¹ s ⁻¹ (×N _A)	0.0298	0.1103	0.2117	0.1067	0.3248	0.5645	0.1832	0.5446	0.8620
N ₂ × TOF _{Surface} /m ⁻² s ⁻¹ (×N _A)	0.000618	0.002289	0.004394	0.001782	0.005428	0.009433	0.002834	0.008426	0.013337
TOF _{Redox} /s ⁻¹	18.81	69.56	133.55	26.06	79.36	137.90	29.31	87.15	137.95

References

- [1] T. Bryk, T. Demchuk, N. Jakse, J. F. Wax, *Front. Phys.* 2018, **6**, 6.
- [2] Blochl, C. J. Forst, J. Schimpl, *B Mater. Sci.* 2003, **26**, 33-41.
- [3] J. P. Perdew, K. Burke, M. Ernzerhof, *Phys. Rev. Lett.* 1996, **77**, 3865.
- [4] G. Mills, H. Jónsson, *Phys. Rev. Lett.* 1994, **72**, 1124.
- [5] K. Mathew, R. Sundararaman, K. Letchworth-Weaver, T. A. Arias, R. G. Hennig, *J. Chem. Phys.* 2014, **140**, 084106.
- [6] P. P. R. M. L. Harks, F. M. Mulder, P. H. L. Notten, *J. Power Sources* 2015, **288**, 92-105.
- [7] O. Muller, D. Lutzenkirchen-Hecht, R. Frahm, *Rev. Sci. Instrum.* 2015, **86**, 093905.
- [8] B. Ravel, M. Newville, *J. Synchrotron. Radiat.* 2005, **12**, 537-541.